AN ACTIVE CONTOUR APPROACH FOR SEGMENTATION OF INTRA-RETINAL LAYERS IN OPTICAL COHERENCE TOMOGRAPHY IMAGES

by

Azadeh Yazdanpanah
B.Sc., Shahid Bahonar University of Kerman

THESIS SUBMITTED IN PARTIAL FULFILLMENT OF
THE REQUIREMENTS FOR THE DEGREE OF

MASTER OF APPLIED SCIENCE

In the
School of Engineering Science

© Azadeh Yazdanpanah 2010

SIMON FRASER UNIVERSITY

Fall 2010

APPROVAL

Name: **Azadeh Yazdanpanah**

Degree: **Master of Applied Science**

Title of Thesis: **An Active Contour Approach for Segmentation of Intra-Retinal Layers in Optical Coherence Tomography Images**

Examining Committee:

    Chair: **Dr. Shahram Payandeh, P. Eng.**
Professor – School of Engineering Science

_____

Dr. Marinko V. Sarunic, P. Eng.
Co-senior Supervisor
Assistant Professor – School of Engineering Science

_____

Dr. Ghassan Hamarneh
Co-senior Supervisor
Associate Professor – School of Computing Science

_____

Dr. Parvaneh Saeedi, P. Eng.
Internal Examiner
Assistant Professor – School of Engineering Science

Date Defended/Approved: December   9   2010

ii

Declaration of
Partial Copyright Licence

The author, whose copyright is declared on the title page of this work, has granted to Simon Fraser University the right to lend this thesis, project or extended essay to users of the Simon Fraser University Library, and to make partial or single copies only for such users or in response to a request from the library of any other university, or other educational institution, on its own behalf or for one of its users.

The author has further granted permission to Simon Fraser University to keep or make a digital copy for use in its circulating collection (currently available to the public at the "Institutional Repository" link of the SFU Library website <www.lib.sfu.ca> at: <http://ir.lib.sfu.ca/handle/1892/112>) and, without changing the content, to translate the thesis/project or extended essays, if technically possible, to any medium or format for the purpose of preservation of the digital work.

The author has further agreed that permission for multiple copying of this work for scholarly purposes may be granted by either the author or the Dean of Graduate Studies.

It is understood that copying or publication of this work for financial gain shall not be allowed without the author's written permission.

Permission for public performance, or limited permission for private scholarly use, of any multimedia materials forming part of this work, may have been granted by the author. This information may be found on the separately catalogued multimedia material and in the signed Partial Copyright Licence.

While licensing SFU to permit the above uses, the author retains copyright in the thesis, project or extended essays, including the right to change the work for subsequent purposes, including editing and publishing the work in whole or in part, and licensing other parties, as the author may desire.

The original Partial Copyright Licence attesting to these terms, and signed by this author, may be found in the original bound copy of this work, retained in the Simon Fraser University Archive.

Simon Fraser University Library
Burnaby, BC, Canada

ABSTRACT

Optical Coherence Tomography (OCT) is a non-invasive, depth-resolved imaging modality that has become a prominent ophthalmic diagnostic technique. We present a novel segmentation algorithm based on Chan-Vese's energy-minimizing active contours to detect intra-retinal layers in OCT images. A multi-phase framework with a circular shape prior is adopted to model the boundaries of retinal layers and estimate the shape parameters using least squares. We use a contextual scheme to balance the weight of different terms in the energy functional. The results from various synthetic experiments and segmentation results on rat OCT images are presented, demonstrating the strength of our method to detect the desired layers with sufficient accuracy even in the presence of intensity inhomogeneity. Our algorithm achieved an average Dice similarity coefficient of 0.84 over all segmented layers, and of 0.94 for the combined nerve fiber layer, ganglion cell layer, and inner plexiform layer, which are critical layers for glaucomatous degeneration.

Keywords: Biomedical imaging, Image segmentation, Level set, Optical Coherence Tomography (OCT), Retina, Shape, Active contours, Energy minimization

To my parents, Soraya and Sohrab …
To Ali, my best friend …
for their immeasurable spiritual support and love

ACKNOWLEDGEMENTS

To my supervisors, Dr. Marinko Sarunic and Dr. Ghassan Hamarneh, my extreme gratitude for your continuous supervision, encouragement and for introducing me to the word of biomedical computing and medical imaging as well as sharing your profound knowledge and intriguing expertise in this filed. Your understanding and flexibility helped me shape my own path as a graduate student.

Additionally, I would like to extend thanks to the other members of my thesis committee, Dr. Parvaneh Saeedi and Shahram Payandeh for their invaluable comments and suggestions on the development of my thesis.

I want to thank all my peers in Biomedical Optics Research Group and Medical Image Analysis Lab for their support. I would also like to thank Benjamin Smith in particular for his invaluable helps and inspiration.

I would like to thank my parents. You have supported me, without question and qualm, through every twist and turn. If it were not for both of you, I would not be who I am today.

Finally, last but certainly not least, I would like to thank my husband, Ali, for his love and support.

TABLE OF CONTENTS

LIST OF FIGURES

LIST OF TABLES

GLOSSARY

ACWOE   The classical Chan–Vese's active contours.

ACWOE-S   ACWOE with shape constraint only.

ACWOE-SW   Active Contours without Edge with Shape constraint and contextual Weights.

AMD   Age-related Macular Degeneration. It is an eye disease and impairs the retina at the back of the eye.

A-scan   Axial scans measure the backreflection or backscattering versus depth.

B-scan   B-scan are generated by performing a series of A-scan by transversally scanning the beam across the sample.

CFL   Courant–Friedrichs–Lewy . A necessary convergence condition while numerically solving a partial differential equation.

DSC   Dice Similarity Coefficient. A Jaccard index used to measure the similarity of sample sets.

en face   An image which is created by axial summation of 3D OCT data.

FDOCT   Fourier domain Optical Coherence Tomography.

GCL   Ganglion Cell Layer. mostly ganglion cell bodies.

GVF   Gradient Vector Flow. An active contour model that introduced by Xu using a vector field for image segmentation.

HD   Hausdorff Distance. Used to determine how far two

sample sets are from each other.

INL	Inner Nuclear Layer. Cell bodies of bipolar cells, horizontal cells, amacrine cells, interplexiform neurons, Müller cells, and some displaced ganglion cells.
IOP	Intraocular pressure.
IPL	Inner Plexiform Layer. Synaptic connections between bipolar cell axons and ganglion cell dendrites.
IS/OS	Photoreceptor layer of retina. The outer and inner segments of rods and cones.
NGI	The combined nerve fiber layer, ganglion cell layer, and inner plexiform layer (NFL+GCL+IPL).
NFL	Nerve Fiber Layer. Ganglion cell axons.
OCT	Optical Coherence Tomography. A non-invasive, depth-resolved imaging modality which uses low coherence light to provides subsurface morphological or structural information of a sample.
ONL	Outer Nuclear Layer. Rod and cone cell bodies.
OPL	Outer Plexiform Layer. Synapses between photoreceptor cells and cells from the inner nuclear layer.
RPE	Reginal Pigment Epithelium. A single layer of pigmented hexagonal cells in retina.
SDF	Signed Distance Functions. The distance function captures the distance from any point in the image domain to the object boundary and assigns this distance to that point's location.
SDOCT	Spectral Domain Optical Coherence Tomography.
SLD	Super Luminescent Diode light source.
SSOCT	Swept-Source Optical Coherence Tomography.

SVM   Support Vector Machine. A supervised learning
               methods, used for classification and regression
               analysis.

1. INTRODUCTION

Retinal degenerative diseases are known as a major cause of untreatable blindness in the world. Optical Coherence Tomography (OCT) is a relatively new, non-invasive, depth resolved imaging modality that has become a prominent ophthalmic diagnostic technique and can be used to visualize the retinal cell layers in order to detect and monitor a variety of retinal diseases, including Age-related Macular Degeneration (AMD), diabetic retinopathy and glaucoma [1], [2]. OCT can be also adapted for imaging rodent eyes in order to complement medical research and gene therapy to combat retinal degeneration [3]-[7]. Due to the vast amount of data provided by OCT scanners, automated tools for the analysis of these images become critical for extracting useful information from the acquired data. This thesis develops and evaluates an automated intra-retinal layer segmentation in OCT images, which plays a crucial role in studying the retinal degenerative diseases.

1.1. Research Motivation

Visual impairment is a global problem affecting about 160 millions of people worldwide, of whom ~37 millions are blind. A total of 81% of blind people are more than 50 years of age. The second leading cause of vision loss is glaucoma (12.3%), next to cataract (47.8%) [8]. Cataract is any opacification of the lens, i.e. it affects the front of the eye, while glaucoma impairs the retina and

optic nerve head at the back of the eye. Glaucoma has no early warning signs, causing substantial damage unless diagnosed early. In contrast, cataract can be treated adequately since it is usually noticeable by the patient in the early stage.

Glaucoma is a chronic, irreversible eye disease, which is correlated with the gradual loss of the retinal ganglion cells and their optic nerve axons. In addition to the major factor of elevated intraocular pressure (IOP), the risk of glaucoma is higher due to increasing age, black race, family history of glaucoma, myopia, and abnormal blood pressure. There are several types of glaucoma. The two most common are angle closure glaucoma, having sudden and acute onset, and primary open angle glaucoma, which is more common and tends to be progress at a slower rate [9].

Successful treatment of glaucoma is highly dependent on early diagnosis of this disease. The clinical assessment of glaucoma includes measurements of IOP via tonometry, the optic nerve head examination using indirect ophthalmoscopy and optic disc stereo biomicroscopy. The other key components consist of the anterior-chamber angle examination using anterior segment slit lamp biomicroscopy or gonioscopy, and assessing the retinal nerve fiber layer using the imaging techniques such as scanning laser polarimetry (GDx), confocal scanning laser ophthalmoscopy (e.g., heidelberg retinal tomography or HRT), and OCT.

Among the imaging modalities used in diagnosis of ocular diseases, OCT provides images with higher resolution and is the first imaging technique allowing the delineation of retinal substructure *in vivo*. In addition, OCT can provide direct

information on the dimensions of retinal structure (e.g. thickness) and can detect changes bellow the threshold for detection on a standard ophthalmoscopic examination of the *en face*. These advantages make OCT a more appropriate tool in diagnosis of glaucoma since this chronic disease affects the thickness of retinal structures as well, i.e. thinning of retinal nerve fiber and ganglion cell layer. *In vivo* measurement of the retinal layer thickness is important for studying retinal diseases. OCT can be also adapted for imaging rodent eyes to study the small animal model of diseases in order to understand the disease mechanisms, monitoring the disease progression, and response to therapies [3]-[7]. Rodent models have contributed to a wide range of scientific achievements for a significant number of ocular diseases.

Due to the vast amount of image data provided by OCT scanners, the need and potential impact of image analysis methods are high. Automated intra-retinal layer segmentation creates a quantitative tool enabling ophthalmologists to diagnose and monitor retinal diseases. In this thesis, we propose a novel active contour based algorithm to address the segmentation of intra-retinal layers in OCT images. We evaluate this approach on various synthetic data and OCT images of rats. Intra-retinal layer segmentation has several applications. One example is the extraction of individual layer properties, such as thickness, shape, or texture, to understand what features from OCT images are associated with visual dysfunction in retinal diseases. Other examples include the earlier detection of macular area ganglion cell loss in cases of concurrent optic nerve

swelling and creating an atlas including information about normal layer properties and typical inter-subject variations [10].

1.2. The Eye and the Retina

The eye is a special sense organ in human body, which is approximately a sphere consisting of two parts: the cornea and the sclera. The cornea is the smaller sphere anteriorly, with the greater curvature than the sclera, which constitutes the larger sphere. The dimension of the eye is 25 *mm* with the volume of 6.5 *ml* and has many specialized structures and tissues [11]. Figure 1-1 shows a schematic cross sectional of the human eye structure. Travelling through the cornea, pupil, and the lens, light is focused on the retina lining the inner surface at the back of the eye. Retina is a light-sensitive tissue forming a circular disc with diameter of approximately 42 *mm* in total and thickness of 0.5 *mm*. The retinal consists of two regions: central and peripheral. The peripheral retina is the
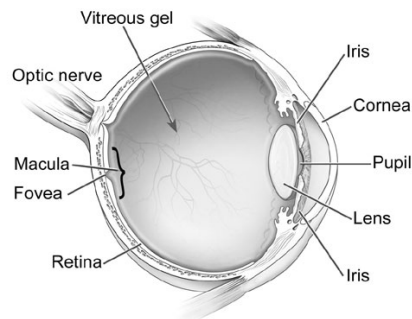
Figure 1-1. Schematic cross sectional of the human eye anatomy (National Eye Institute, National Institutes of Health Ref #: NEA09).

large portion of the retina, which is rich in rods and detects gross shapes and motion. The central retina is, however, designated for visual acuity and is cones

dominate and has more ganglion cells per area. A darkened region in the central retina is called macula which is ~5.5 *mm* in diameter. The fovea, the centre of the macula, is a slightly oval-shaped, blood vessel-free reddish spot, located approximately 4.5-5 *mm* to the left of the optic disc. The optic nerve head, or optic disc, is a circular to oval white area where ganglion cell axons accumulate and exit the eye. The horizontal diameter of the disc is ~1.7 *mm* and the vertical diameter is ~1.9 *mm* [11]. Striking the retina, light initiates a cascade of chemical and electrical events triggering nerve impulses, sent to various visual centres of the brain through the optic nerve. As schematically represented in Figure 1-2, the retina is composed of several layers of neurons interconnected by synapses, from outermost to innermost [10], [11]:

- Reginal Pigment Epithelium (RPE): single layer of pigmented hexagonal cells.
- Photoreceptor layer: the Outer and Inner Segments (IS/OS) of rods and cones.
- Outer Nuclear Layer (ONL): rod and cone cell bodies.
- Outer Plexiform Layer (OPL): synapses between photoreceptor cells and cells from the inner nuclear layer.
- Inner Nuclear Layer (INL): cell bodies of bipolar cells, horizontal cells, amacrine cells, interplexiform neurons, Müller cells, and some displaced ganglion cells.
- Inner Plexiform Layer (IPL): synaptic connections between bipolar cell axons and ganglion cell dendrites.

- Ganglion Cell Layer (GCL): mostly ganglion cell bodies.

- Nerve Fiber Layer (NFL): ganglion cell axons.
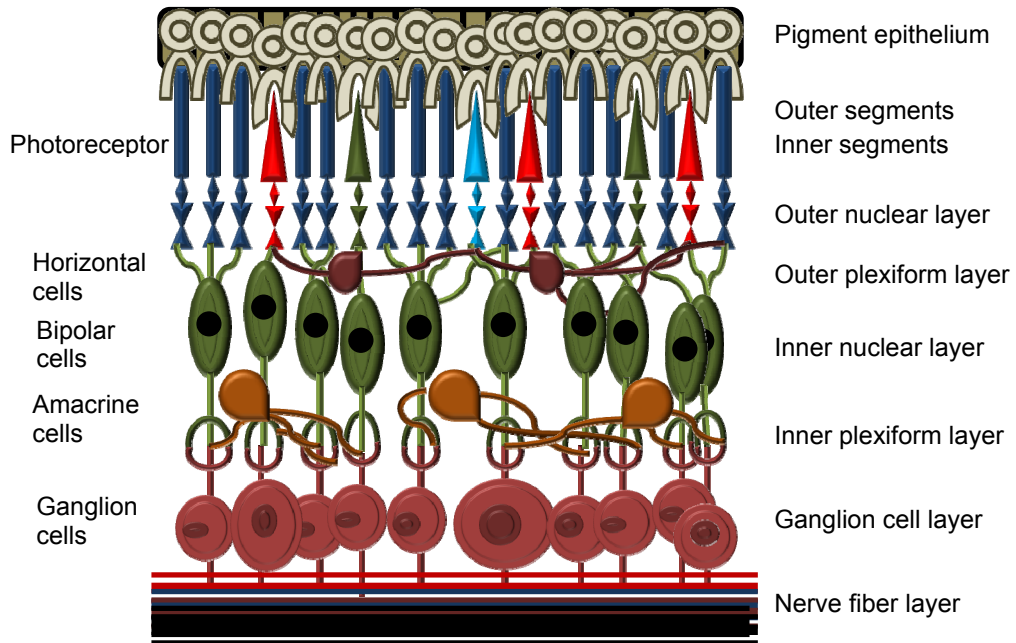
Figure 1-2. Retinal layers, from outermost to innermost [12].

The visual system of the rat as a rodent is very similar to other mammalian species. Figure 1-3 shows a schematic of a rat eye. Rat has relatively small eyes having an axial length of about 6-8 *mm*. Similar to other nocturnal mammals, the rat eye is characterized by relatively large cornea and lens, where the lens accounts for about 60% of the axial length [13]. The basic functional structure of the rat retina resembles that of the human; however, the rat retina does not have a fovea centrials and does not have the corresponding variation in the thickness in retinal layers. The retina has a total thickness of about 230 ± 10 *µm* and consists of the following layers similar to human: NFI, GCL, IPL, INL, OPL, ONL, IS/OS, and RPE.
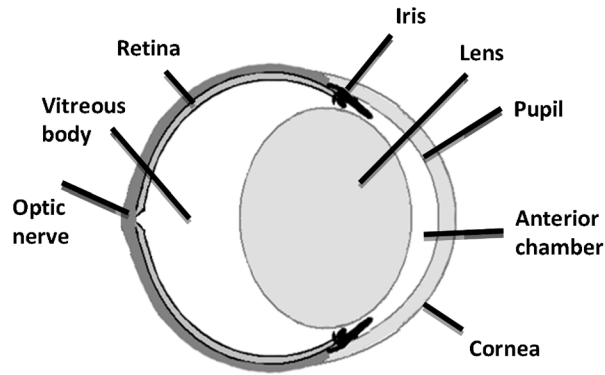
Figure 1-3. Schematic cross sectional of the rat eye anatomy [14].

1.3. Review of the Related Works on Intra-Retinal layer Segmentation

In this section, we provide a review on automated approaches employed in OCT segmentation [15]-[24]. Some methods rely on pixel-level edge detection algorithms [25] or are based on performing a 1-D intensity peak detection procedure for each A-scan [16]-[18]. This could potentially lead to detection of broken boundaries and erroneous edges. Moreover, since OCT images are highly corrupted by speckle noise, these algorithms required pre-processing to reduce the effect of noise. The de-noising procedure, however, affects the sharpness of the edges, which subsequently reduces the segmentation performance. The aforementioned methods do not consider the intensity inhomogeneity in the image which can lead to inaccurate segments and inability to detect all layers. In [19] and [20], a Support Vector Machine (SVM) algorithm is used to perform segmentation of retinal layers. By considering the mean intensity of six neighbors at each voxel, the SVM approach can handle noisy OCT images. However, this approach is not only dependent on a user to mark a set of points for the purpose of training and segmentation but also fails to

7

segment the layers accurately if the feature and background points are not chosen properly. Further, SVM is computationally expensive and is not able to segment all layers at the same time. Mishra *et al.* propose a two-step kernel based optimization scheme to segment intra-retinal layers [26]. To simultaneously delineate the retinal layers, they perform a set of local optimization strategies, but it is unclear how the algorithm considers the interaction between the segmented regions to avoid the ambiguity in the segmentation results. In addition, they did not provide any quantitative evaluations of the algorithm. A method to segment the retinal pigment epithelium (RPE) using a polarization sensitive optical coherence tomography (PS-OCT) [27] is demonstrated by [28]. Their method relies on the depolarizing property of the RPE and it requires a PS-OCT instrument. Garvin et al. [21] and Haeker et al. [22], [23] model the segmentation problem as finding the minimum s–t cut of a geometric graph. The cost function is the summation of an edge-based term and one or more region-based terms. They have developed a sequential approach to segment the intra-retinal layers. First, the three easier-to-segment surfaces are found (upper surface of NFL and upper and lower surfaces of OS). The position of the previous segmented surfaces is incorporated into the cost function to delineate the remaining surfaces. The problem arises when the previous surfaces are segmented inaccurately. This may result in an inaccurate segmentation of the remaining surfaces. Recently, Garvin et al. [24] have proposed an extension to their algorithm. By learning the surface feasibility constraints using a training set, they can segment the layers in two stages

incorporating both the image edge and true regional information in the cost function.

1.4. Contributions

The major contributions of this thesis are as follows:

- Develop and validate a new method, termed Active Contours without Edge with Shape constraint and contextual Weights (ACWOE-SW), to address the segmentation of intra-retinal layers in OCT images. This novel segmentation method:

  o Incorporates the shape prior based on expert anatomical knowledge of the retinal layers into a multi-phase, level-set Mumford–Shah model.

  o Employs temporally and specially adaptive (i.e. contextual) weights to balance the cost terms in the energy functional.

  o Compensates the intensity inhomogeneity in OCT images which can lead to inaccurate segments and inability to detect all the layers.

- Validate the performance of ACWOE-SW for segmentation of intra-retinal layers using 80 OCT images from 7 rats. Also, the quantitative comparisons between our proposed method (ACWOE-SW) and the classical Chan–Vese's active contours (ACWOE) and the ACWOE with shape constraint only are reported. Manual segmentation of the retinal layers is used as the gold standard.

- Assess ACWOE-SW method quantitatively with respect to the noise, algorithm parameters, and the initial curve in order to demonstrate its robustness. The computation time of the algorithm is also evaluated.

- Report experimental longitudinal study of acute neuro-degeneration in rats to perform a pilot analysis on the NGI (NFL+GCL+IPL) complex thickness over 14 days post-axotomy.

The work in this thesis was published in the *Medical Image Computing and Computer-Assisted Intervention* (*MICCAI*) [14] and an extended version has been recently accepted for publication in the *IEEE Transactions on Medical Imaging* (*TMI*) [29]. The longitudinal study of acute neuro-degeneration was published in Optics Express [30].

1.5. Thesis Organization

This dissertation develops and evaluates a new algorithm based on the Chan–Vese active contours without edges [31] to address the segmentation of intra-retinal layers in OCT images. Chapter 2 reviews the principles of the Spectral Domain OCT (SDOCT) as the image modality used in this study. Chapter 3 provides an introduction to active-contour-based approaches and the level set methods for image segmentation. The methodology of our work is described in detail in Chapter 4. Chapter 5 provides quantitative longitudinal study of acute neuro-degeneration in rat using the developed segmentation

approach. We provide the summary and conclusions of this dissertation along with a discussion of the future research in Chapter 6.

2. OPTICAL COHERENCE TOMOGRAPHY

This chapter reviews the state of the art in Optical Coherence Tomography (OCT). After a brief introduction to spectral domain OCT, the image acquisition procedure is described. Finally, some properties of the rodent retina OCT images are addressed.

2.1. Introduction

Optical coherence tomography is a non-invasive, noncontact imaging modality which uses low coherence light to provides subsurface morphological or structural information of a sample. The resolution in OCT systems approaches that of histology; the lateral resolution depends on the sample arm optical configuration (typically 10-20 μm) and the axial resolution is dependent only on the source spectrum (typically ~4 μm) [32]. OCT is a powerful tool for ophthalmic imaging and can be used to visualize the retinal cell layers in order to detect and monitor a variety of retinal diseases. This technology can be also adapted for imaging rodent eyes in order to understand the disease mechanisms and response to therapies to provide better clinical management of retinal diseases.

The standard OCT system is based on a Michelson interferometer that interferes light back scattered or reflected from a sample with reference light. In Fourier domain (FD) OCT, the optical path length difference between sample and reference reflections is obtained by the frequency of the interferometic fringes as

a function of the source spectrum without movement of the reference arm. The location of scatterers are revealed by the magnitude of the Fourier transformation of interferograms fringes observed when sample and reference waves coherently interfere. Two types of FDOCT system have been demonstrated based on the combination of the source and detector used. Spectral-domain (or spectrometer-based) systems referred to as SDOCT uses the low coherence source but a spectrometer in the detector arm spatially disperses the interferometric signal spectrum across an array-type detector. In Swept-Source systems (SSOCT), however, using a wavelength swept source laser the spectrum is acquired in a single detector. In this thesis, only SDOCT systems will be discussed.

2.2. Image Acquisition

The images used in this study were acquired using a custom spectrometer based Fourier domain SDOCT system. The SDOCT system used a continuous Super Luminescent Diode (SLD) light source operating at a central wavelength of 826 nm with a spectral bandwidth full width half maximum of 72 nm. The axial resolution was nominally ~4 μm (in air). The interferometer was constructed using a 2×2 fiber coupler with a 70/30 splitting ration, providing 30% of the source light to the sample arm. In this configuration, 70% of the light collected in the sample arm of the interferometer was directed back to the spectrometer, improving the attainable signal to noise ratio. The high speed spectrometer was a custom design constructed using a 1200 lines/mm transmission diffraction grating. The detector was a 1024 element high speed Gigabit Ethernet (GigE) camera from Dalsa (Waterloo, Canada), with 14 μm square pixels and was

operated at a line rate of 20 KHz for imaging. The reference arm consisted of a collimating lens, a reflective attenuator (metallic neutral density filter), and a mirror. The sample arm comprised of a collimating lens, a beam expander and an objective lens with scanning provided by a pair of galvanometric mounted mirrors (galvos) (Cambridge Technology).

2.2.1. Spectral-Domain OCT (SDOCT)

This section focuses on theory of the SDOCT systems. An optical layout of a typical SDOCT system, schematically illustrated in Figure 2-1, consists of a superluminescent source, Michelson type interferometer, and CCD camera in the detector arm. Light from the source is divided by a 2×2 fibre coupler into the sample and reference arm. The recombined beam interfere at the detector to produce fringes corresponding to the optical path length mismatch between the two paths, Δz. For the case of a single reflector in the sample, and for a system without dispersion, the signal acquired at the detector, I_D, can be expressed as [33],[34]:

$$I_D(k) = S(k)\left[R_R + R_S + \left(2\sqrt{R_R R_S} \cos(2\Delta z k) \right) \right],$$ (2-1)

where $S(k)$ is the intensity profile of the source with Gaussian spectrum, R_R and R_S represent the reflectivity of the sample and reference object. The location of reflector in the sample is extracted by taking the Fourier transform of equation (2-1):
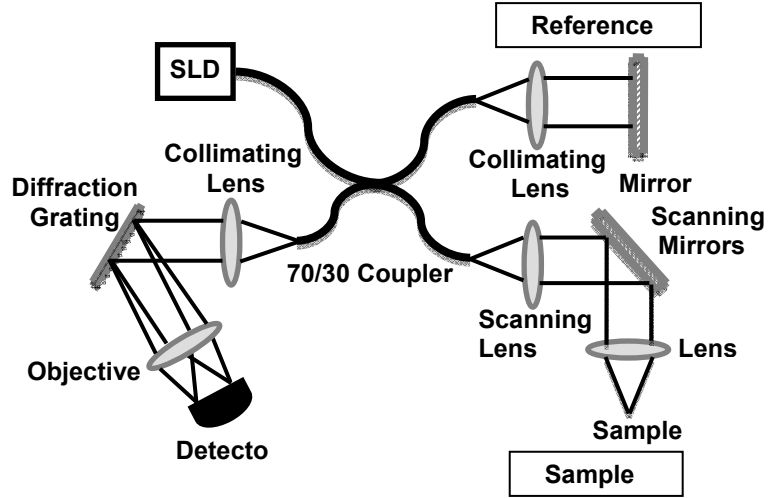
Figure 2-1. Schematic of SDOCT system consists of a superluminescent source, Michelson type interferometer, and CCD camera in the detector arm.

$$\hat{I}_D(z) = \hat{S}(z)\left[\left(R_R + R_S\right)\delta(z) + 2\sqrt{R_R R_S}\left(\delta(z - 2\Delta z) + \delta(z + 2\Delta z)\right)\right], \qquad (2\text{-}2)$$

where $\delta(\cdot)$ is the Dirac delta function, and $\hat{S}(\cdot)$ is the Fourier transform of the source spectrum. The results from equation (2-2) include three terms. The first term is referred to as DC offset, resulting from the non-interfering components of the sample and reference arms. The second and third terms represent the location of the reflector and its complex conjugate, respectively.

2.2.2. Scanning Scheme

The A-scan is a depth-resolved reflectivity profile of the sample at a single point. A cross-sectional image, or B-scan, is created by transversally scanning the beam across the sample and acquiring an axial scan at each location (i.e. multiple A-scans). Volumetric imaging is performed by acquiring sequential cross-sectional images by scanning the spot across the surface of the sample (acquiring multiple B-scans). For rat retinal imaging, the scanning protocol was a

dense raster scan that acquired 3-D OCT data consisting of 400 images with 512 axial scans each in the fashion shown in Figure 2-2, where the fast scan axis is in the X-direction, and the slow scan axis (adjacent frames) is in the Y-direction. The dashed lines represent a B-scan and correspond to a scan rate of ~30 frames per second (30 ms), with each axial scan (A-scan) consisting of 1024 points. The dimension of each OCT scan is 1024 $\times$ 512 $\times$ 400 voxels covering 1.7 $\times$ 4.0 $\times$ 4.0 mm^3 and the voxel size is 1.67 $\times$ 7.80 $\times$ 10.00 μm^3.
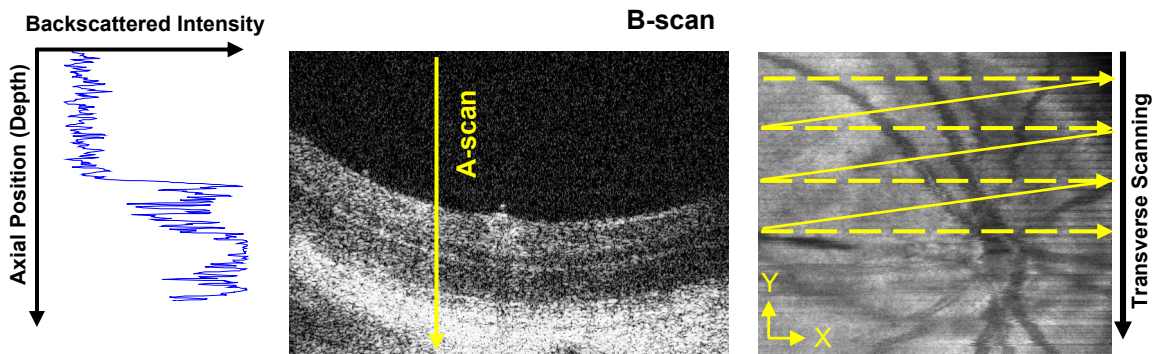
Figure 2-2. Scanning sequence of the galvo in volumetric image acquisition. Axial scans (A-scans) measure the backreflection or backscattering versus depth. Cross-sectional images (B-scan) are generated by performing a series of axial scans by transversally scanning the beam across the sample. Volumetric imaging is performed by raster scanning a series of two-dimensional images (B-scans).

2.2.3. Post-Processing Steps

Real-time data acquisition was performed using a custom software package developed by Biomedical Optics Research Group (BORG) at SFU called OCTViewer. The software package was written in C++ for rapid image acquisition, post-processing and display of two dimensional images. Post-processing was performed in real-time and included DC subtraction of the reference arm spectrum, re-sampling of the interferometric data from linearly sampled in wavelength space to linear sampling in wavenumber space, fast

Fourier transform, second and third-order dispersion compensation, and contrast and brightness enhancement. Dispersion imbalance between the sample and reference arms of the interferometer was compensated numerically by correcting the phase of the interference fringe pattern.

2.3. Rodent Retina OCT Images

The image acquisition was performed on rat retina using the SDOCT system described in Section 2.2. Figure 2-3 shows the morphological depth information in a multi-layer sample, the retinal layers acquired from a rat. The adjacent layers are visualized as horizontal bright and dark bands due to intrinsic differences in optical properties (e.g. reflectivity). The retinal layers encompasses the following layers: NFL, GCL, IPL, INL, OPL, ONL, and IS/OS. This interpretation of the layers in rodent retina OCT images is consistent with histology as can be seen in Figure 2-3. The NFL, IPL and OPL are known to be highly light-scattering, while INL and ONL are relatively low-scattering layers. NFL, GCL, and IPL are not consistently resolvable in most of the OCT images. This may be due to polarization effects of the NFL coupled with the thinness of this layer. For these reasons, we consider NFL, GCL, and IPL together as a combined layer, termed NGI. Similar to human retinal images, the photoreceptor retinal pigment epithelium complex consists of three reflective layers: IS, OS, and RPE.
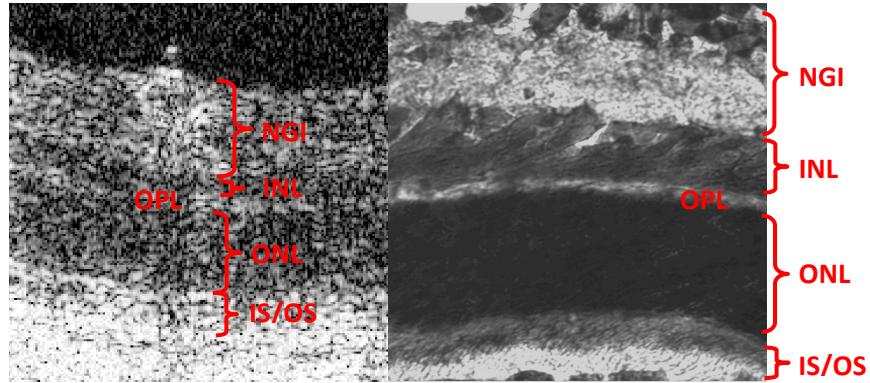
Figure 2-3. An OCT B-scan image presenting a horizontal retinal cross-section with the labels indicating the retinal layers in comparison with a histological section.

OCT images are contaminated with speckle noise, resulting from constructive and destructive interferences of backscattered waves and appearing as a random granular pattern [35], [37]. In addition to the optical properties (e.g. multiple scattering and phase aberrations of the propagating light beam) and sample motion, speckle is influenced by the size and temporal coherence of the light source and the aperture of the detector. Speckle is a multiplicative noise and modelled as a Rayleigh distribution [38]. Applying a logarithmic transformation converts the multiplicative speckle noise to an additive white Gaussian noise [38]-[41]. To consider the correlation nature of the speckle, a correlated Gaussian model can be also used [38]. It is worth noting that the size of the speckle in relation to the retinal layers is substantial, particularly in the OPL and hard to eliminate, as it caries information about tissue micro-structure.

Similar to other medical data, OCT images also suffer from different types of artifacts. Evident in the B-scan is the presence of intensity inhomogeneities (the red circles in Figure 2-4 (b)), bright saturation/shouldering artifact (the red rectangle in Figure 2-4 (c)). The intensity inhomogeneity, as a general artifact in
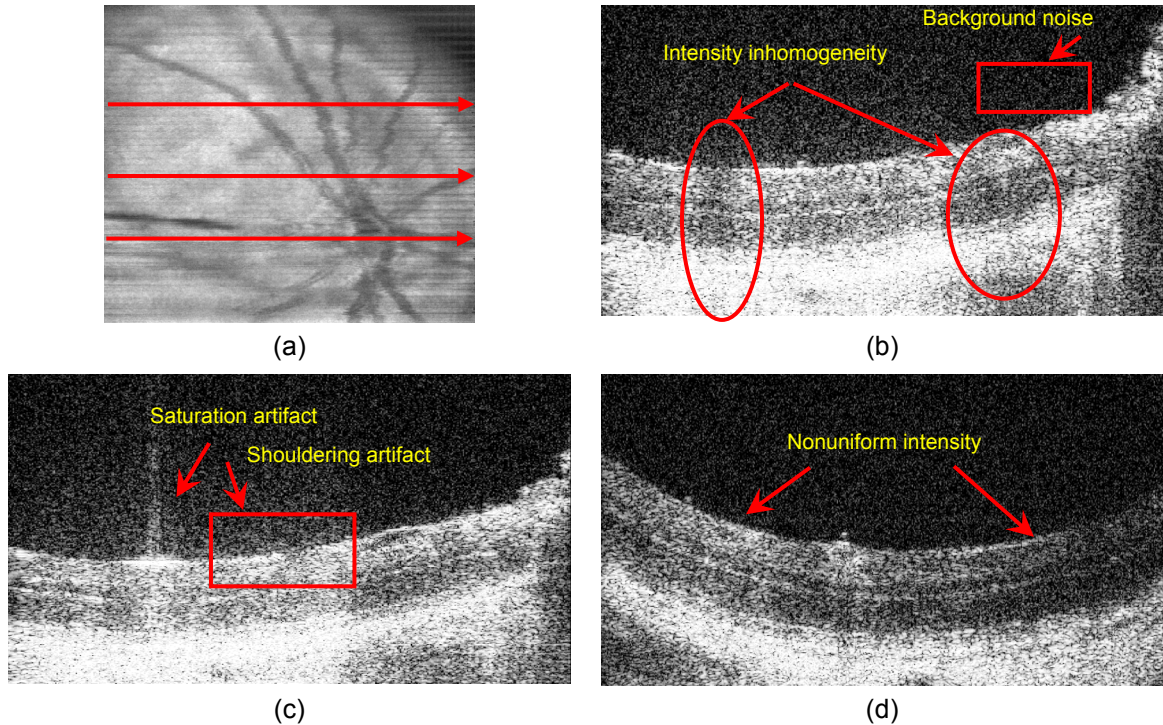
Figure 2-4. Artifacts in retinal OCT images. (a) An *en face* image, created by axial summation of 3D OCT data. (b)–(d) Typical OCT B-scan image presenting a horizontal retinal cross-section with different types of artifacts: the intensity inhomogeneity, the saturation artifact, and the intensity nonuniformity along the layers within a B-scan. The red arrows on the *en face* correspond to the region from which the images were taken.

OCT retina images [42], [44], results from the absorption and scattering of light by the blood vessels in the retina. These inhomogeneities are vertical, or nearly perpendicular to the layers, because of imaging geometry. The bright saturation artifact, observed as vertical lines in the images, is due to high back scattering intensity from the vitreo-retinal interface. The optical power is highest at the vitreo-retinal interface because it has not been scattered or absorbed in the retinal layers, and the higher detected intensity leads to bright "shoulders" in the axial direction of the Fourier transformed images. Furthermore, the intensity may not be uniform along the layers within a B-scan as presented in Figure 1-2(d) resulting from nonuniformity of the signal strength during scan acquisition (e.g. because of defocusing, decentration, or shaking galvo).

<div align="center">(a)   (b)</div>
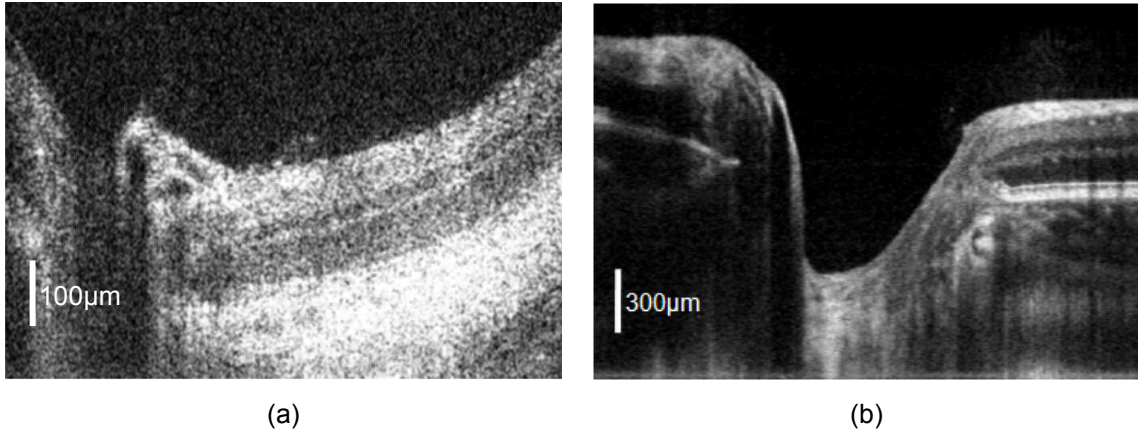
Figure 2-5. A typical rat B-scan image (a) in comparison with human B-scan image (b).

Another source of distortion in OCT imaging is the motion artifact which may result from animal motion, some physiological phenomena (such as breathing, cardiac motion, pulsation, and blood flow), or environmental changes including mechanical vibration, sound waves, and temperature drift, to name a few. The axial motion of the sample results in corruption of the signal (SNR) due to the phase washout, and the transverse sample motion leads to decreasing of SNR as well as degradation in transverse resolution, causing blurriness in OCT images.

In addition, imaging the retina in rodents is significantly more challenging than for human subjects due to the small size of the rodent eyes. The high radius of curvature of the rodent cornea introduces optical aberrations which blur the focal spot at the retina. Also, rodent retinal layers are thinner than those in humans, approaching the resolution of standard OCT systems. As a result, the OCT cross sectional images of rodent retina are of a lower quality than can be acquired in human subjects. Figure 2-5 compares a typical rodent OCT B-scan with that of human (the acquisition procedure was described in detail in [45]).

2.4. Chapter Summary

This chapter presented some background on OCT with emphasis on SDOCT, used to acquire data in this thesis. The details of the image acquisition procedure including our SDOCT optic setup, the scanning scheme, and the custom software OCTViewer were explained.

In the next chapter, an overview of active contour approaches for image segmentation will be provided with the objective of motivating the development of our novel multiphase intra-retinal layer segmentation method, presented in Chapter 4 and evaluated using the OCT data described in the current chapter.

3. ACTIVE CONTOURS METHODS FOR IMAGE SEGMENTATION

Image segmentation is a key step in analysis and interpreting of image data and its main goal is to partition an image into non-overlapping, constituent regions, which are homogeneous with respect to one or more characteristics or features.

Among the wide variety of segmentation algorithms, active contours-based methods have received considerable interest, particularly in the medical imaging. In active contour methods, first introduced by Kass, Witkin, and Terzopoulos [46], a contour defined within an image domain evolves under the influence of internal and external forces (i.e. energy forces), through the solution of an energy minimization problem or dynamic force formulation. The internal forces specify the tension or smoothness of the contour during deformation while the external forces are derived from image data to move the curve toward the salient boundary of an object or other desirable image features. External forces vary from local image gradients to global region statistics such as means and standard deviations. Energy forces can be also based on other quantities such as contour orientation or position [47].

This chapter provides a general overview of several active contour based image segmentation methods. Section 3.1 illustrates the concept of level set methods, as a tool for implementing the curve evolution. In Section 3.2, the

traditional active contour (snake) and some of its extensions are reviewed, addressing the shortcomings with the original approach. Section 3.3 discusses the Chan-Vese active contour and its advantages over edge-based methods. Finally, some of the unique challenges in segmentation of OCT images are addressed in Section 3.4, which motivate our proposed segmentation algorithm.

3.1. Level Set Methods

In the problem of curve evolution, a contour can be tracked by straightforward numerical schemes such as Lagrangian approaches or by more sophisticated numerical schemes such as the Eulerian level set methods.

In the Lagrangian representation, the contour is parameterized discretely into a set of interconnected control points. Each control point advances to its new location under the influence of the forces to represent the updated curve front. This approach suffers from several drawbacks. First, the time steps must be impractically small to achieve a stable evolution. The contour must be re-parameterize during the evolution process to faithfully recover the object boundary since the initial contour may be significantly different in size and shape from the desired object boundary (e.g. the control points tend to come together near high curvature regions if there is no re-parameterizing procedure). The Lagrangian approach is not also able to handle the topological changes of the contour. As the contour splits or merges, ad hoc techniques [48], [49] are required to make this approach work.

(a) Original Curve

(b) Original hyper-surface

(c) Curve changed topology after a few iteration

(d) Hyper-surface showing topological changes in contour at later steps in evolution
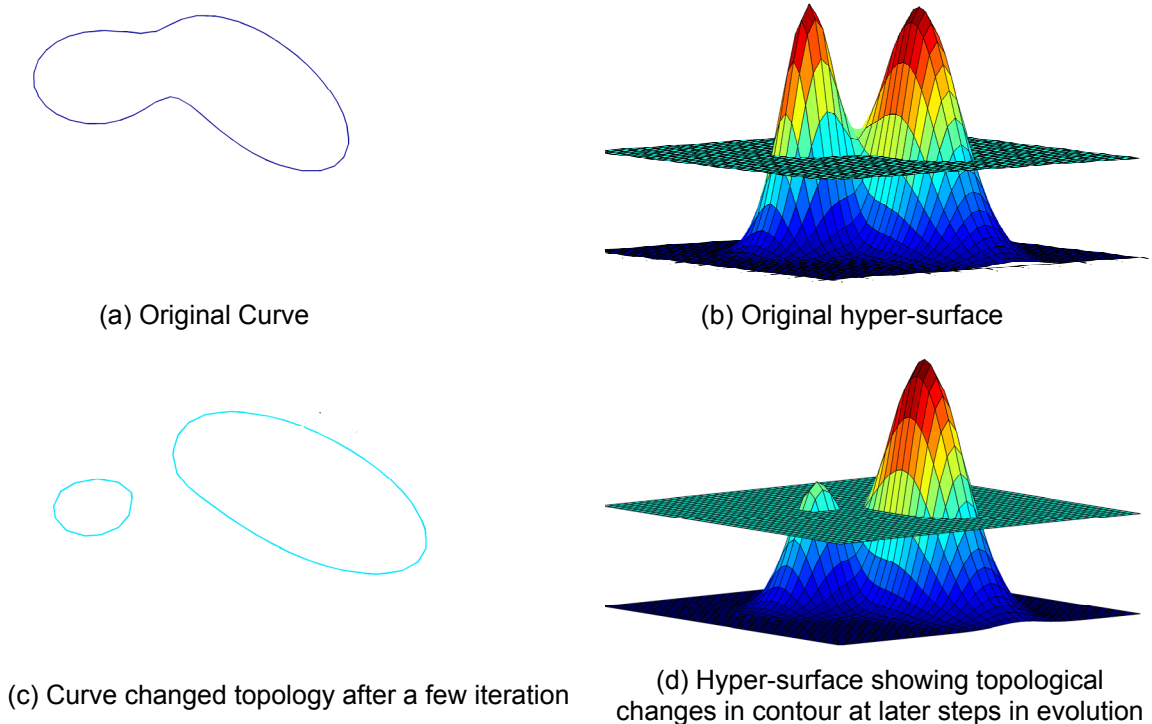
Figure 3-1. An example of embedding a curve as a level set. A curve (left) and its level set representation (right) are shown. The curve is given by the zero level set of the hyper-surface in higher dimension. As the hyper-surface evolves, the zero level set splits into two curves.

Osher and Sethian [50], [51] developed the level set technique for evolving curve in the Eulerian framework. In the level set representation of a contour, the curve is embedded as a zero-level set of a function or hyper-surface that has a larger dimension than the curve (usually the same dimension of the image). The curve is manipulated through the changes in shape, orientation, and location of the embedding hyper-surface implicitly, based on approximations to the equations of motion. Following the topological changes (splitting and merging) of the curve becomes much easier with the level set technique because the hyper-surface remains defined and differentiable (smooth) everywhere. For the illustration purpose, consider Figure 3-1 where each row describes the

contour and its corresponding hyper-surface. As we can see in Figure 3-1(c), the topology of the curve changes quite easily while the level set function evolves.

In two dimensions, a level set method represents the curve C as a zero-level set of a function $\phi : \mathbb{R}^2 \times [0, \infty) \to \mathbb{R}$:

$$C(t) = \{(x, y) \in \Omega \mid \phi(x, y, t) = 0\}, \tag{3-1}$$

Starting with an initial level set function $\phi(t = 0)$, the evolution of the curve is given by its zero level set moving according to the desired flow of the contour. A typical example of a level set function is a signed distance function with respect to the curve. By defining the sign of the level set function to be positive inside and negative outside the contour, the unit normal vector $\vec{\mathbf{n}}$ of the contour C is defined as:

$$\vec{\mathbf{n}} = \frac{\nabla \phi}{|\nabla \phi|} \tag{3-2}$$

The curvature κ, which measures how fast the curve bends at any spot along the contour, is defined as:

$$\kappa = div(\frac{\nabla \phi}{|\nabla \phi|}) = \frac{\phi_{xx}\phi_y^2 - 2\phi_x\phi_y\phi_{xy} + \phi_{yy}\phi_x^2}{\left(\phi_x^2 + \phi_y^2\right)^{3/2}} \tag{3-3}$$

The curvature of the contour is positive if the unit normal vectors diverge and negative where the unit normal vectors converge.

3.2. Edge-Based Active Contours

The classical snake or active contour model [46] turns the segmentation problem into an energy minimization problem. A snake is a parameterized curve $C(s) = [x(s)\ y(s)]^T$, $s \in [0,1]$ which is influenced by external forces and images forces that push it towards features such as lines and edges. The snake energy functional is a weighted summation of internal and external forces:

$$E(C) = E_{int}(C) + E_{ext}(C) \qquad\qquad (3\text{-}4)$$

The internal force E_{int} comes from the shape of the snake to control the smoothness and the continuity of the contour:

$$E_{int} = \alpha \int_0^1 |C'(s)|\,ds + \beta \int_0^1 |C''(s)|\,ds \qquad\qquad (3\text{-}5)$$

where $C'(s)$ and $C''(s)$ are the first and second derivative of the contour with respect to parameter *s*, respectively. The weighted positive parameters α and β specify the elasticity and stiffness of the snake, respectively. In practice, α and β are often chosen to be constants.

The external force E_{ext} emanates from the image data as an integral of a potential energy function $P(x, y)$ along the contour:

$$E_{ext} = \int_0^1 P(x,y)ds \qquad (3\text{-}6)$$

The potential energy function $P(x,y)$ must take small values at the salient features of interest to minimize the external force. A typical potential energy function, depending on the gradient of the image I, is:

$$P(x,y) = \frac{1}{1 + |\nabla G_\sigma(x,y) * I(x,y)|^p}, \quad p \geq 1 \qquad (3\text{-}7)$$

Where $G_\sigma * I$ is the convolution of image I with a Gaussian function $G_\sigma(x,y)$ with variance σ^2. The potential energy function $P(x,y)$ is positive in homogeneous regions and approaches zero at the edges. From the calculus of variation, the contour C which minimizes the energy functional E defined in (3-4) must satisfy the following Euler-Lagrange equation [46]:

$$\alpha \frac{\partial^2}{\partial^2 s} C(s) - \beta \frac{\partial^2}{\partial^2 s} (\frac{\partial^2 C(s)}{\partial^2 s}) - \nabla P(c(s)) = 0 , \qquad (3\text{-}8)$$

To solve the Euler-Lagrange equation, suppose an initial estimate of the solution is available and the contour C is a function of time t and parameter s, i.e. $C(s,t)$. Then, the evolution equation is obtained as:

$$\frac{\partial C(s,t)}{\partial t} = \alpha \frac{\partial^2}{\partial^2 s} C(s,t) - \beta \frac{\partial^2}{\partial^2 s} (\frac{\partial^2 C(s,t)}{\partial^2 s}) - \nabla P(C(s,t)) , \qquad (3\text{-}9)$$

The solution is found when the contour $C(s,t)$ stabilizes, i.e. $\partial C(s,t)/\partial(t) = 0$ [52]. Minimizing the snake energy functional is not straightforward. Different parameters including weight of force terms and iteration step should be defined appropriately. The initial snake must be placed close

enough to the true boundary of the object. In addition, the Euler-Lagrange solution suffers from numerical instability.

Many efforts have been made to address these problems. Cohen *et al.* [53] proposed balloon snake approach to allow the snake avoid spurious isolated edge points. An additional pressure force is added to the external force component of equation (3-6) by considering the curve as a balloon which is inflated:

$$E_{ext} = -\nabla P(x,y) + E_{const}\vec{\mathbf{n}} \, , \tag{3-10}$$

where E_{const} is an arbitrary constant and $\vec{\mathbf{n}}$ is the unit normal vector on the contour front. However, adjusting the strength of the balloon force is difficult, i.e. the balloon force must be large enough to pass through weak edges and overcome the noise but small enough not to crush a true boundary. Moreover, since the balloon force is not derived from the image, the snake may continue to inflate at the points where the legitimate boundary is missing or weaker than the inflation force.

Xu and Prince [54], [55] proposed the Gradient Vector Flow (GVF) snake method. In this method, a new external force was introduced to extend the capture range of the snake. The diffusion of the gradient vectors of the edge map (new external force) is maximum near the edges and decreases as moving away from the true edges (see Figure 3-2 (b)), pulling the contour that is located far away from the true edges. In the original snake, however, contour evolves based on the edge map (gradient of the image), which only exists in the neighbourhood

of the true edges (see Figure 3-2 (c)). Therefore, if the initial contour is located far a way from the true edges, the evolving contour might stop at undesirable superior edges or not move at all.
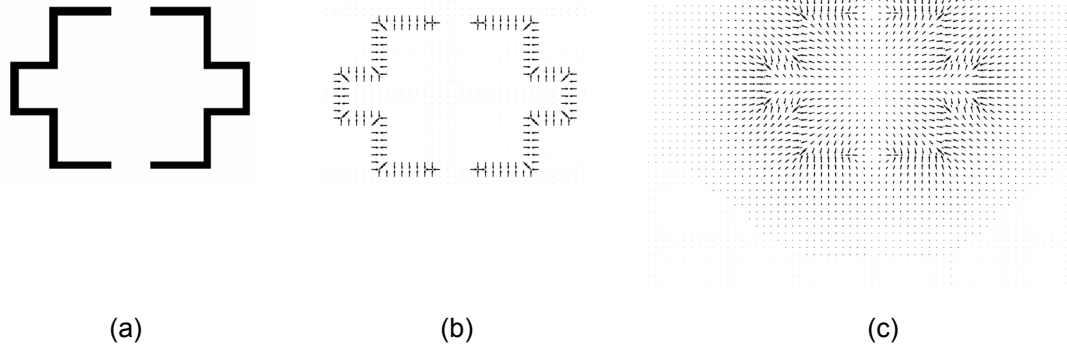
Figure 3-2. Potential force field of edge map: (a) Original image, (b) Gradient of the edge map, and (c) GVF field.

Malladi et al. [56] and Caselles et al. [57] proposed edge-based geometric active contours based on the theory of curve evolution where the contour is represented by Eulerian level set methods, allowing for automatic topological changes. The contour evolves only based on geometric measures such as the curvature and the normal vectors, and therefore there is no need for re-parameterization which is the case in parametric active contours. Other active contour methods based on level sets were proposed in [58]-[60] using a local edge-based energy (e.g. image gradient) to stop the curve.

All these classical snakes and active contour models are edge-based and depend on the image gradient to stop the curve evolution. Therefore, they work well for objects that have well-defined edge map. However, if the image is very noisy or the object boundary is occluded which is very frequent in medical

imaging, the contour may pass through the boundaries resulting in incorrect segmentation. To overcome this drawback, the region-based methods are proposed which use global information instead of local information and are less sensitive to the initial location of the contour as well as noise.

3.3. Region-Based Active Contours

Chan and Vese [31] describe a new active contour scheme, which does not use edges, and combine an energy minimization approach with a level set based solution. Considering a given image $I : \Omega \rightarrow \mathbb{R}^2$, and C as a contour in the image domain Ω, the Mumford-Shah functional [61] for the segmentation of a piecewise constant model can be rewritten as follows according to [50]:

$$
\begin{aligned}
F_\varepsilon(c_1, c_2, C) = {} & \mu \cdot Length(C) \\
& + \lambda_1 \int_{inside(C)} |I(x,y) - c_1|^2 \, dxdy + \lambda_2 \int_{outside(C)} |I(x,y) - c_2|^2 \, dxdy
\end{aligned}
\tag{3-11}
$$

where μ, λ_1, and λ_2 are fixed positive parameters to weight the different terms in the energy function, and c_1 and c_2 are the average intensity value of the image I inside and outside of the curve C, respectively. Representing C as a zero level set of the level set function ϕ, minimizing the functional (3-11) is equivalent to solving the following partial differential equation [31]:

$$
\frac{\partial \phi}{\partial t} = \delta_\varepsilon(\phi) \left[\mu \, div \left(\frac{\nabla \phi}{|\nabla \phi|} \right) - \lambda_1 (I - c_1)^2 + \lambda_2 (I - c_2)^2 \right], \quad \phi(0, x, y) = \phi_0(x, y)
\tag{3-12}
$$

where div $(\cdot)$ denotes the divergence and $\delta_\varepsilon = \varepsilon / \pi(\varepsilon^2 + \phi^2)$ is the regularized delta function [31]. The first term in equation (3-12), the divergence term is the

internal force, which depends on the curve itself such as its curvature or smoothness [50]:

$$div\left(\frac{\nabla\phi}{|\nabla\phi|}\right)\delta_\varepsilon(\phi) = \kappa(C), \qquad (3\text{-}13)$$

where $\kappa(C)$ is the curvature of the contour C. Therefore, equation (3-12) corresponds to the curve evolution:

$$\frac{\partial C}{\partial t} = \left[\mu\,\kappa - \lambda_1(I-c_1)^2 + \lambda_2(I-c_2)^2\right]\vec{\mathbf{n}}, \qquad (3\text{-}14)$$

where $\vec{\mathbf{n}}$ denotes the exterior normal of contour C. The evolution of contour C results from the last two terms in equation (3-12). Based on the current position of the contour, term $\lambda_1(I-c_1)^2\delta_\varepsilon(\phi)$ can be smaller or greater than term $\lambda_2(I-c_2)^2\delta_\varepsilon(\phi)$. If $\lambda_1(I-c_1)^2\delta_\varepsilon(\phi)$, square difference between intensity value of pixels on the contour from c_1, is greater than $\lambda_2(I-c_2)^2\delta_\varepsilon(\phi)$, square difference between intensity value of pixels on the contour from c_2, the contour will move outward, and vice versa the contour will move inward (i.e. when $\lambda_1(I-c_1)^2\delta_\varepsilon(\phi)$ is smaller). The evolution of the contour will continue until these two terms become equal, which results in segmenting the image into two constant-intensity regions.

Chan-Vese active contour model, in contrast to edge-based models, is less sensitive to the initial location of the contour and noise. In addition, the topological changes of the contour are handled automatically through the level set implementation. Figure 3-3 (a) shows an example of a noisy image segmented using Chan-Vese active contour. The interior contour of the torus is

31

(a)

(b)
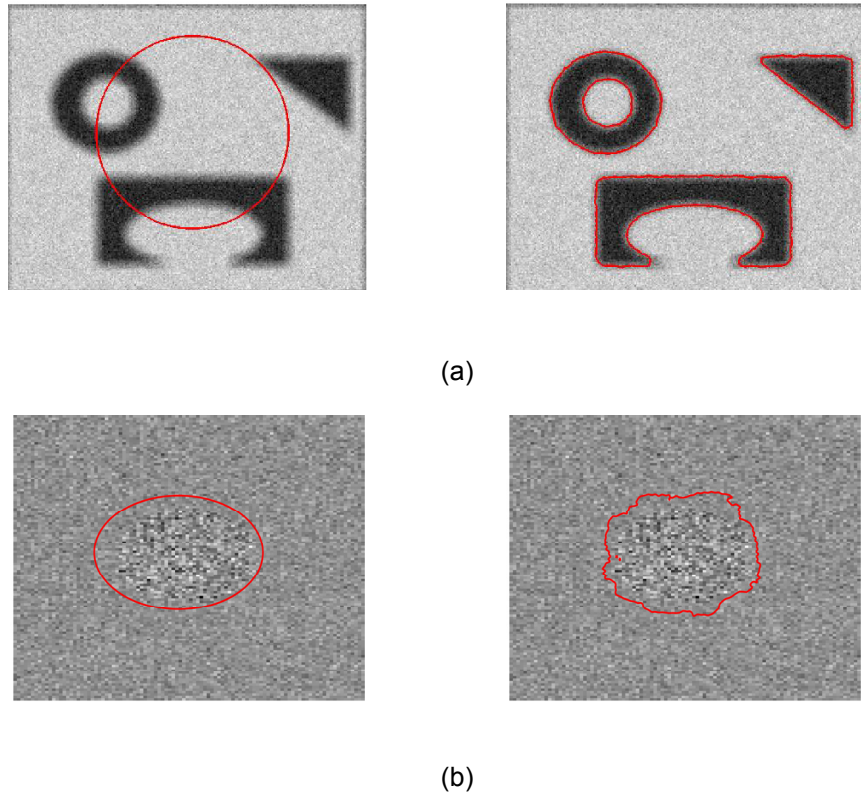
Figure 3-3. Segmentation results of Chan-Vese active contour: (a) A noisy image with an interior contour which is segmented with the algorithm. (b) The case that object and background have the same mean but different variances. The algorithm fails to segment the object.

automatically segmented due to the level set implementation of the method. However, Chan-Vese active contour has its own limitations. For example, it fails to segment the images which are not piecewise-constant, such as objects with the same mean but different variances or statistically inhomogeneous objects. As an instance, we refer to Figure 3-3 (b) where the algorithm fails to segment the object with the same mean as the background but different variance. This shortcoming is due to the fact that Chan-Vese active contour is a reduced case of the Mumford-Shah model, so-called "minimal partition problem". That is, the intensity of desired object is modelled as the average intensity of the image inside the corresponding contour.

3.4. Problem in Retina OCT Images

In this section, we introduce the principles of our novel segmentation algorithm to address the problems inherent in OCT images posing some unique challenges for segmentation.

As discussed in Section 2.3, rodent OCT images are of lower quality than human images due to optical aberrations resulting from the high radius of cornea curvature and thinner retinal layers comparable to the resolution of standard OCT systems. Also, evident in the B-scan is the presence of intensity inhomogeneities and bright saturation artifact presenting additional challenges for segmentation algorithms. OCT images are highly corrupted by speckle noise as well. The size of the speckle in relation to the retinal layers is substantial and presents an obstacle for image segmentation algorithms.

OCT provides images with micrometer resolution which is suited to ophthalmic applications. For the FDOCT system used in this work, the axial resolution is nominally ~4 μm (in air) resulting in pixel size of 1.67 μm. Therefore, since the precision of segmentation algorithms is limited by the resolution of the imaging system, in order to quantitatively analyze the pathological changes in retinal layers, the needed precision for a segmentation algorithm would be ~1-2 pixels.

Addressing the abovementioned problems, we have developed a new algorithm based on the Chan–Vese active contours without edges to simultaneously delineate the retinal layers in OCT images. Our multi-phase segmentation algorithm incorporates a shape prior term resembling the

morphology of the retinal layers to improve the segmentation accuracy in the presence of artefacts. Introducing an adaptive contextual scheme makes the algorithm more robust when the image information is not sufficient to accurately detect the layers, as in the low contrast OCT images. The proposed method is region-based and performs well on noisy OCT images. The implicit implementation of the contour based on level set resulting in a continuous metric space provides the precision of sub-pixels for the proposed algorithm. In the next chapter, the details of our proposed methodology are presented.

3.5. Chapter Summary and Conclusions

The present chapter reviewed the active contour methods. Active contour models start from an initial estimation of the curve based on the higher level knowledge and the initial curve is refined through optimization approach (e.g. minimizing an energy functional). The curve can be represented explicitly by a set of marker points or implicitly based on level set methods. The level set methods offer several advantages over conventional parametric models, including flexible topology, no need for re-parameterization, and concise descriptions of differential structure. During the curve evolution, image data, initial estimate, desired contour properties, and knowledge-based constraints are considered. The image data can be derived form the local image information (edge-based) or from the global image information (region-based). Edge-based models are greatly affected by noise and low contrast images and they are very sensitive to the initial placement of the curve. In contrast, region-based active contours are more robust to the noise and initial placement because they use the

statistics of the entire image. However, they fail to segment object with intensity inhomogeneity or object that is not piecewise constant. Due to the problem in OCT images, the existing method fail to delineate the retinal layers. Therefore, we proposed a novel active contour based segmentation method to overcome these problems which is elaborated in the next chapter.

4. MULTI-PHASE SEGMENTATION: ACTIVE CONTOUR WITHOUT EDGE PLUS SHAPE AND WEIGHT APPROACH

In this chapter, we propose a novel algorithm based on the Chan–Vese active contours without edges [31] to address the segmentation of intra-retinal layers in OCT images. To the best of our knowledge, we are the first to segment OCT data using a multi-phase, level-set Mumford–Shah model that incorporates a shape prior based on expert anatomical knowledge of the retinal layers, avoiding the need for training. Our approach has four main features. First, it can segment all intra-retinal layers simultaneously due to the multi-phase property of the algorithm. Second, we incorporate a shape prior term that enables the algorithm to accurately segment retinal layers, even where the region-based information is missing, such as in inhomogeneous regions. The predominant source of these inhomogeneities is the blood vessels in the retina which absorb light strongly, reducing the backscattered optical intensity of the underlying retinal tissue. Third, our method is region-based and performs well on noisy OCT images. Finally, our algorithm is robust and avoids the re-initialization problem that is associated with the level set approach [62] .

To achieve the needed accuracy and robustness for our application, we employ temporally and spatially adaptive (i.e. contextual) weights that balance the cost terms of our energy functional. In contrast to earlier methods for spatially adaptive regularization that rely on reliability and curvature measures [63]-[65],

our proposed adaptive weights not only control the effect of the shape prior spatially based on gradient of the image, but also vary temporally based on simulated annealing schedule. We include concentric circles as a shape prior which mimic the geometrical retinal layer structure, and estimate the shape parameters using least squares. The methodology of our work is described in detail in Section 4.1. We apply the algorithm to 80 retinal OCT images acquired for both eyes of seven rats. In Section 4.1.4, we explain the minimization process of the energy functional that designed in Section 4.1. The numerical implementation of our method is explained in Section 4.2 using the first order convex scheme within the level set frame work. The process of data acquisition is briefly discussed in Section 4.4. To evaluate the segmentation method, in Section 4.5, we compare the automated segmentation with the ground truth manual segmentation using three different and complementary error metrics: Dice Similarity Coefficient (DSC), Hausdorff Distance (HD) and absolute thickness differences. In addition, we compare the proposed method with two other active-contour-based approaches. The work in this chapter has been recently accepted for publication in the *IEEE Transactions on Medical Imaging (TMI)* [29][1].

4.1. Energy Functional

Our objective is to segment a given OCT image, $I : \Omega \longrightarrow \mathbb{R}^2$, defined on the image domain, into R disjoint sub-regions, which accurately label the retinal

---

[1] © 2010 IEEE. Reprinted, with permission, from IEEE Transactions on Medical Imaging, Segmentation of Intra-Retinal Layers from Optical Coherence Tomography Images using an Active Contour Approach, A. Yazdanpanah, G. Hamarneh, B. Smith, and M. Sarunic.

layers. The decomposition of the image I will be modeled using the level set framework as a set of $R-1$ Signed Distance Functions (SDFs), ϕ. The distance function captures the distance from any point in the image domain to the object boundary and assigns this distance to that point's location. The SDF assigns opposite signs to the interior versus exterior of the object. Formally, the SDF is an implicit function with positive values in the interior region Ω^+, negative values in the exterior region Ω^-, and zero on the boundary $\partial\Omega$ with the property that $|\nabla\phi|=1$ [66]. Further details of this representation are provided in Section 4.1.1. To determine a segmentation, we developed a variational algorithm that minimizes the following energy functional:

$$E(\phi) = \lambda_I E_I(\phi) + \lambda_S E_S(\phi) + E_R(\phi).$$
(4-1)

Each term of the energy functional captures a separate aspect of the problem. The first term, E_I, incorporates region-based information derived from the image. E_S incorporates the prior shape knowledge of the anatomy of the retinal layers. The third term, E_R is a regularizing term which keeps region boundaries smooth and encourages each ϕ to be a SDF. That is, E_R is defined as a weighted summation of two terms, E'_R and E''_R, as follows:

$$E_R = \lambda'_R E'_R + \lambda''_R E''_R.$$
(4-2)

Positive valued parameters λ_I, λ_S, λ'_R and λ''_R weight the different terms in the energy functional.

4.1.1. Region-Based Term

The first term of equation (4-1) follows the work of Chan and Vese [31] and encourages each region of the segmentation to have an approximately constant intensity. The intensity of the ith sub-region will be approximated by the constant μ_i, and the spatial extent will be represented by a characteristic function χ_i.

$$E_I = \sum_{i=1}^{R} \int_{\Omega} (I(x,y) - \mu_i)^2 \, \chi_i(x,y) \, dxdy. \qquad (4\text{-}3)$$
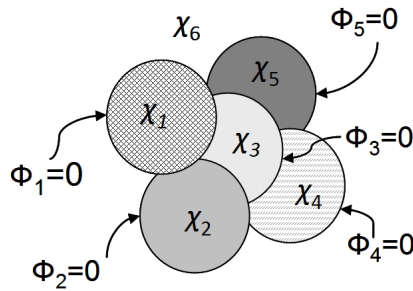
Figure 4-1.The segmentation of the image domain into multiple regions (χ_i, $i = 1,...,6$) is represented by set operations on regions defined by the zero contours of the signed distance functions (ϕ_i, $i = 1,...,5$). The first region, χ_1, consists of the region inside of ϕ_1. The final region, χ_6, is the region outside of all zero contours. Intermediate regions, χ_i, are defined as the regions outside of all ϕ_j, $j < i$, and inside ϕ_i.

By definition, each characteristic function takes the value 1 inside the region, and 0 outside. Following the approach of Mansouri *et al.* [67], each χ_i is represented using the level set method as a function of $R-1$ SDFs, ϕ. Simply, χ_i is the region inside the zero contour of the ith SDF, and outside all previous SDFs zero contours. The final region χ_R, is the region outside the zero contours

of all SDFs. Figure 4-1 shows the χ_i for a case of six regions of segmentation (five SDFs). Using this partitioning, we guarantee unambiguous segmentation of R regions using $R-1$ SDFs. The characteristic function for the ith region is defined as follows, using the Heaviside step function, H, and the Kronecker delta function, δ [68]:

$$\chi_i = H(\phi_i)^{1-\delta[R-i]}\left[\prod_{k=1}^{i-1}(1-H(\phi_k))\right]. \tag{4-4}$$

4.1.2. Shape Prior Term

OCT images may not always be piecewise constant. Intensity inhomogeneity may exist in regions due to the "shadows" cast by retinal blood vessels which absorb and scatter light strongly. To compensate for these intensity inhomogeneities, we incorporated a shape prior term. Based on prior knowledge of retinal anatomy, a circular shape prior is used to model the retinal layer boundaries, and assists the algorithm when region-based information is insufficient to segment a layer accurately. In our model, each circular prior will share a common center point, but has a unique radius. The squared distance from a point, (x, y), to the shape prior constraining the ith boundary, can be defined as:

$$D_i(x,y) = [(x-c_x)^2 + (y-c_y)^2 - r_i^2]^2, \tag{4-5}$$

where (c_x, c_y) is the common center of the prior terms encouraging concentric layers, and r_i is the radius of the circular prior of the interface between the ith and the $(i+1)^{th}$ layer.
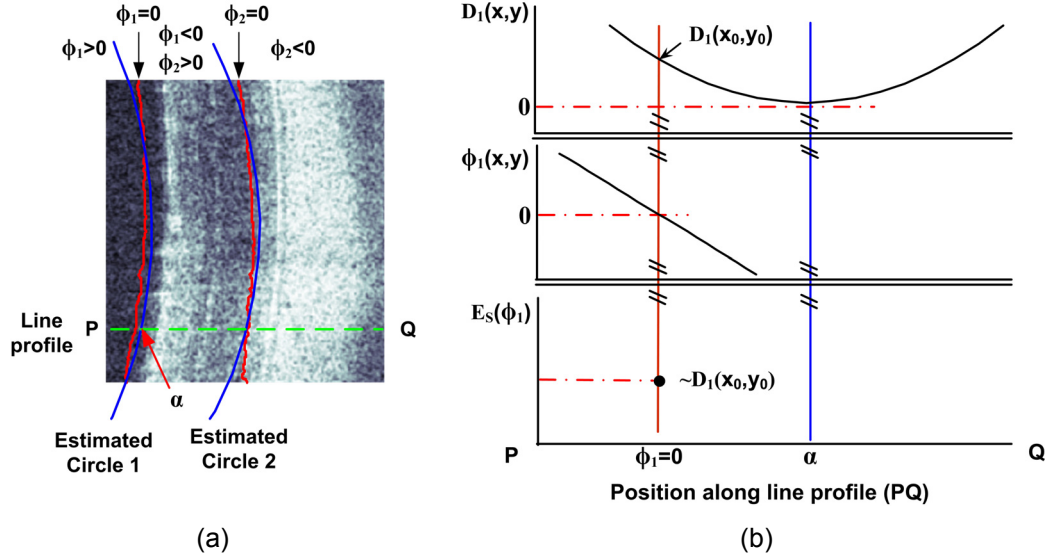
Figure 4-2. Shape prior energy functional. (a) A typical scheme of the shape prior and the signed distance function. (b) The values of $D_1(x, y)$, $\phi_1(x, y)$, and $E_s(\phi_1)$ from P to Q along the line profile. The distance between $\phi_1 = 0$ and α in (b) is exaggerated for illustration.

For each SDF ϕ_i, a shape constraint encourages the region boundary (the zero level set) to lie on a circle, minimizing the squared distance of the zero level set to the prior. Consequently, the shape term in the energy functional is:

$$E_S = \sum_{i=1}^{R-1} \int_\Omega D_i(x, y) \delta(\phi_i(x, y)) | \nabla \phi_i(x, y) | \, dxdy. \qquad (4\text{-}6)$$

The term $\delta(\phi_i(x, y)) | \nabla \phi_i(x, y) |$ selects out the zero level set of ϕ_i using the Dirac delta function $\delta(\cdot)$. This causes the shape term to have a non-zero value only on the region boundaries, and the term E_S is minimized when ϕ_i lies exactly on the circular shape.

41

Figure 4-2 (a) shows an example configuration of the shape prior and the signed distance function, overlaid on a typical OCT image. The red arcs represent the zero level sets of SDFs ϕ_1 and ϕ_2. The blue lines indicate two circular shape priors with center (c_x, c_y) and radii r_1 and r_2. The dotted green line is a "line profile" providing sampling of this information (shape priors, SDFs, image data) along the path from P to Q. Figure 4-2 (b) shows the values of $D_1(x, y)$, $\phi_1(x, y)$, and $E_s(\phi_1)$, as we move from P to Q along the line profile in Figure 4-2 (a). The point labeled α indicates the point along the line profile which is on the edge of the shape prior, corresponding to distance of r_1 from (c_x, c_y). As we move from P to Q, the value of D_1 decreases as we approach the boundary (at distance r_1) and then increases again as we move away. For ϕ_1, its value is positive as it approaches the zero level set and then becomes negative as we cross the boundary. This information can be combined to get the E_S term of the energy, i.e. when ϕ_1 is zero (the zero level set), the Dirac delta is 1, and the D_1 term contributes to E_S to give a value.

The shape parameters c_x, c_y, and r_i for E_S are defined using a least square fit, with ϕ_i and μ_i held fixed. For this purpose, the parameter vector $\theta = [c_x\ c_y\ \tau_1\ \tau_2 \cdots \tau_{R-1}]^T$ (where $\tau_i = r_i^2 - c_x^2 - c_y^2$) is estimated such that the error ε in $b = \Psi\theta + \varepsilon$ is minimized, where Ψ and b are determined by points (x, y) lying on $R-1$ boundaries as follows:

$$\Psi = \left[\psi_1, \psi_2, \cdots, \psi_{R-1} \right]^T, \quad b = \left[b_1, b_2, \cdots, b_{R-1} \right]^T. \tag{4-7}$$

Defining the pixels on the ith circle by (x_{ik}, y_{ik}) $(1 \le k \le M_i)$, b_i and ψ_i are

$$b_i = \begin{bmatrix} x_{i1}^2 + y_{i1}^2 \\ x_{i2}^2 + y_{i2}^2 \\ \vdots \\ x_{iM_i}^2 + y_{iM_i}^2 \end{bmatrix}, \psi_i = \begin{bmatrix} V_i & W_i \end{bmatrix}, \tag{4-8}$$

where V_i is defined as

$$V_i = \begin{bmatrix} 2x_{i1} & 2y_{i1} \\ 2x_{i2} & 2y_{i2} \\ \vdots & \vdots \\ 2x_{iM_i} & 2y_{iM_i} \end{bmatrix}. \tag{4-9}$$

Matrix W_i is determined by shifting the columns of the following matrix $i - 1$ times to the right.

$$W_0 = \begin{bmatrix} 1 & 0 & 0 & \cdots & 0 \\ 1 & 0 & 0 & \cdots & 0 \\ \vdots & \vdots & \vdots & \cdots & \vdots \\ 1 & 0 & 0 & \cdots & 0 \end{bmatrix}_{M_i \times R-1} \tag{4-10}$$

Finally, the shape parameters are estimated using least squares:

$$\hat{\theta} = (\Psi^T \Psi)^{-1} \Psi^T b. \tag{4-11}$$

4.1.3. Regularization Term

Regularization terms are added to keep the boundaries of the segmented layers smooth [31], and ϕ_i as a valid SDF. Smooth boundaries are encouraged by adding a contour length term (E'_R), and ϕ_i can be kept close to a SDF by adding the penalty term of Chunming *et al.* (E''_R) [62]:

$$E'_R = \sum_{i=1}^{R-1} \int_\Omega \delta(\phi_i(x,y)) \,|\, \nabla \phi_i(x,y)\,|\, dxdy,$$

$$E''_R = \sum_{i=1}^{R-1} \int_\Omega \frac{1}{2}(|\nabla \phi_i(x,y)|-1)^2 \; dxdy. \tag{4-12}$$

Recalling from (4-2), E_R is the weighted summation of E'_R and E''_R. Therefore, we have:

$$E_R = \sum_{i=1}^{R-1} \int_\Omega \left[\lambda'_R \left(\delta(\phi_i(x,y)) \,|\, \nabla\phi_i(x,y)\,|\, \right) + \frac{\lambda''_R}{2}(|\nabla\phi_i(x,y)|-1)^2 \right] dxdy. \tag{4-13}$$

4.1.4. Minimization of the Energy Functional

By substituting the energy terms defined by (4-3), (4-6), and (4-13) into (4-1), and re-arranging slightly, the minimization problem associated with our model is defined as:

$$\inf_{\mu_i,\varphi_i} E = \int_\Omega \lambda_I \sum_{i=1}^{R} \left[(I-\mu_i)^2 \chi_i \right] + \sum_{i=1}^{R-1} \left[A_i(x,y)\delta(\phi_i) \,|\, \nabla\phi_i \,|\, + \frac{\lambda''_R}{2}(|\nabla\phi_i|-1)^2 \right] dxdy, \tag{4-14}$$

where $A_i(x,y) = \lambda'_R + \lambda_S D_i(x,y)$.

To minimize this functional, we followed the approach of Chan and Vese [31] and performed an alternating minimization. First, we hold the SDFs fixed, and solve for the unknown intensities μ_i:

$$\mu_i = \frac{\int_\Omega I(x,y)\chi_i \, dxdy}{\int_\Omega \chi_i \, dxdy}.$$
(4-15)

Next, holding the intensities fixed, we use the Euler–Lagrange equation with respect to ϕ_i and parameterize the descent direction using an artificial time t. The derivation of the Euler–Lagrange equation corresponding to (4-14) is presented in Appendix A, which results in the following update equation.

$$\frac{\partial \phi_j}{\partial t} = -\lambda_I \sum_{i=1}^{R} (I - \mu_i)^2 \frac{\partial \chi_i}{\partial \phi_j}$$
$$+ \left[\nabla A_j \cdot \frac{\nabla \phi_j}{|\nabla \phi_j|} + A_j \, \mathrm{div}(\frac{\nabla \phi_j}{|\nabla \phi_j|}) \right] \delta(\phi_j)$$
$$+ \lambda''_R \left[\triangle \phi_j - \mathrm{div}\left(\frac{\nabla \phi_j}{|\nabla \phi_j|} \right) \right],$$
(4-16)

where

$$\frac{\partial \chi_i}{\partial \phi_j} = \begin{cases} (-H(\phi_i))^{1-\delta(i-j)} \delta(\phi_j) \times \\ \qquad \prod_{k=1}^{i-1}(1-H(\phi_k))^{1-\delta(k-j)} & i \neq R, j \leq i \\ \\ -\delta(\phi_j)\prod_{k=1}^{i-1}(1-H(\phi_k))^{1-\delta(k-j)} & i = R, j < i \\ \\ \qquad\qquad 0 & i \neq R, j > i \end{cases}$$
(4-17)

Note that, in practice, we use regularized versions of H and δ to obtain a well–defined descent direction. The regularization of Chan and Vese [31] was used:

$$H_\varepsilon(z) = \frac{1}{2}\left(1 + \frac{2}{\pi}\arctan\left(\frac{z}{\varepsilon}\right)\right),$$

$$\delta_\varepsilon(z) = \frac{1}{\pi}\frac{\varepsilon}{\varepsilon^2 + z^2}.$$

(4-18)

4.2. Numerical Implementation

In this section, we present the numerical approximation of the method by using a finite differences scheme. Let h be the spacing step, $x_l = lh$ and $y_m = mh$ denote the grid points (l and m are nonnegative integers and $h > 0$), and Δt be the time step for each iteration. Let $\phi^n_{<l,m>} = \phi^n(n\Delta t, x_l, y_m)$ be an approximation of $\phi(t, x, y)$, with $n \geq 0$, $\phi^0 = \phi_0$, where ϕ_0 is the initial set of signed distance functions. The initial contour is estimated based on three points that are provided by the user (we elaborate on this in Section 4.5). The required finite differences can be approximated as:

$$\Delta^x_+ \phi_{<l,m>} = \phi_{<l+1,m>} - \phi_{<l,m>}, \qquad \Delta^x_- \phi_{<l,m>} = \phi_{<l,m>} - \phi_{<l-1,m>}$$

$$\Delta^y_+ \phi_{<l,m>} = \phi_{<l,m+1>} - \phi_{<l,m>}, \qquad \Delta^y_- \phi_{<l,m>} = \phi_{<l,m>} - \phi_{<l,m-1>}$$

(4-19)

The numerical approximation to (4-16) is as follows:

$$\frac{\phi^{n+1}_{j<l,m>} - \phi^n_{j<l,m>}}{\Delta t} = -\lambda_I \sum_{i=1}^{R}(I_{<l,m>} - \mu_i)^2 \frac{\delta\chi^n_{i<l,m>}}{\delta\phi^n_{j<l,m>}}$$

$$+ \left[\nabla A_{j<l,m>} \cdot \frac{\nabla\phi^n_{j<l,m>}}{|\nabla\phi^n_{j<l,m>}|} + A_{j<l,m>}\,\mathrm{div}\left(\frac{\nabla\phi^n_{j<l,m>}}{|\nabla\phi^n_{j<l,m>}|}\right)\right]\delta(\phi^n_{j<l,m>})$$

(4-20)

$$+ \lambda''_R\left[\Delta\phi^n_{j<l,m>} - \mathrm{div}\left(\frac{\nabla\phi^n_{j<l,m>}}{|\nabla\phi^n_{j<l,m>}|}\right)\right],$$

$$\frac{\delta\chi^n_{i<l,m>}}{\delta\phi^n_{j<l,m>}} = \begin{cases} (-H(\phi^n_{i<l,m>}))^{1-\delta(i-j)}\delta(\phi^n_{j<l,m>})\times \\ \displaystyle\prod_{k=1}^{i-1}(1-H(\phi^n_{k<l,m>}))^{1-\delta(k-j)} & i\neq R, j\leq i \\[3em] -\delta(\phi^n_{j<l,m>})\displaystyle\prod_{k=1}^{i-1}(1-H(\phi^n_{k<l,m>}))^{1-\delta(k-j)} & i=R, j<i \\[3em] 0 & i\neq R, j>i \end{cases} \quad (4\text{-}21)$$

where

$$\mathrm{div}\left(\frac{\nabla\phi^n_{j<l,m>}}{|\nabla\phi^n_{j<l,m>}|}\right) = \frac{1}{h^2}\Delta^x_-\left(\frac{\Delta^x_+\phi^{n+1}_{j<l,m>}}{\sqrt{(\Delta^x_+\phi^n_{j<l,m>})^2/h^2+(\phi^n_{j<l,m+1>}-\phi^n_{j<l,m-1>})^2/(2h)^2}}\right)$$
$$+\frac{1}{h^2}\Delta^y_-\left(\frac{\Delta^y_+\phi^{n+1}_{j<l,m>}}{\sqrt{(\Delta^y_+\phi^n_{j<l,m>})^2/(h^2)+(\phi^n_{j<l+1,m>}-\phi^n_{j<l-1,m>})^2/(2h)^2}}\right) \quad (4\text{-}22)$$

$$\triangle\phi^n_{j<l,m>} = \frac{1}{h^2}\Delta^x_-(\Delta^x_+\phi^n_{j<l,m>})+\frac{1}{h^2}\Delta^y_-(\Delta^y_+\phi^n_{j<l,m>}) \quad (4\text{-}23)$$

$$A_{j<l,m>} = \lambda'_R + \lambda_S D_{j<l,m>}$$
$$\nabla A_{j<l,m>} = \lambda_S\nabla D_{j<l,m>} = \lambda_S\left(\frac{1}{h^2}\Delta^x_+ D_{j<l,m>},\frac{1}{h^2}\Delta^y_+ D_{j<l,m>}\right). \quad (4\text{-}24)$$

Given sufficiently small time steps, subject to the Courant–Friedrichs–Lewy (CFL) condition, convergence of the above iterative process is guaranteed based on a standard result in the theory of numerical methods [66], [69]. Note that we use the method from [70] for the discretization of the divergence operator.

We optimize the segmentation model using an alternating, iterative, minimization over the SDFs, unknown intensities μ_i, and parameter θ of the

shape prior in (4-6). During each iteration, each parameter is updated using (4-16), (4-15) and (4-11) while holding the other two parameters fixed. The algorithm steps are repeated until the maximum number of iterations N is reached. Another possible stopping criterion is checking whether the solution is stationary or not. We choose a large number of iterations such that the stability of the contour is guaranteed as confirmed by the experimental results in Section 4.5. The principal steps of the algorithm are as follows:

I.   Initialize ϕ^0 by ϕ_0, n=0.

II. Estimate parameter θ of the shape prior (concentric circles) by (4-11).

III. Estimate the intensities μ_i by (4-15).

IV. Update ϕ_j^{n+1} by solving the PDE form (4-20).

V. $n=n+1$, and if $n \leq N$, repeat steps II to V.

4.3. Adaptive Weighting of the Energy Terms

Choosing "good" weights for energy terms in segmentation is an open problem, and finding the correct tradeoff that results in a desirable segmentation is usually treated empirically. In this work, we automatically adapt the weights both temporally and spatially, i.e. the weights change with iteration number and along the spatial dimensions. Intuitively, in early iterations, the region-based term should be more dominant, allowing the curve freedom to evolve toward the boundary of each layer. As the algorithm progresses, the shape term becomes more important to assist the algorithm when image information is insufficient to segment the image. Given that our approach is based on Chan–Vese active

contours without edges, reversing this procedure (i.e. fitting the model according to shape prior first, then intensity) would bring about an inaccurate segmentation. It is necessary to focus on detecting regions of homogeneous intensity to reach the vicinity of the correct solution. Only then will the shape prior be useful. Therefore, we define λ_I and λ_S in terms of the nth iteration as mentioned in [71]:

$$\lambda_I(n) = \lambda_I(1) + \frac{n(\lambda_I(N) - \lambda_I(1))}{N},$$

$$\lambda_S(n) = \lambda_S(1) + \frac{\lambda_S(N) - \lambda_S(1)}{\cosh[8(\frac{n}{N} - 1)]}.$$

(4-25)

where N is the total number of iterations. Figure 4-3 shows the plots of λ as a function of iteration.
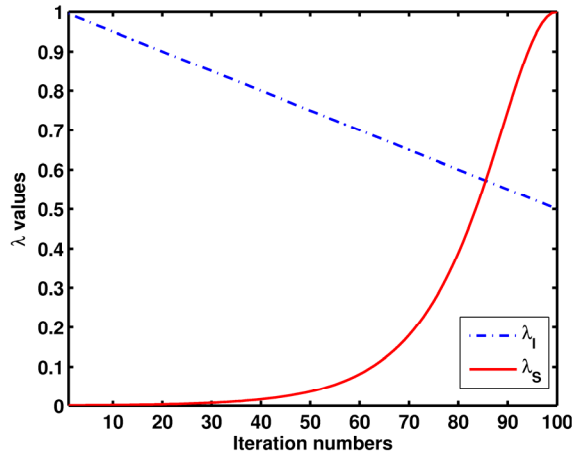
Figure 4-3. Adapting the parameters λ_I and λ_S as a function of iteration. The initial and final values for λ_I and λ_S are set as $\lambda_I(1) = 1$, $\lambda_I(N) = 0.5$, $\lambda_S(1) = 0$, and $\lambda_S(N) = 1$.

We also want the shape term to have a greater effect where image intensity information is missing, as in the inhomogeneous regions. Therefore, contextual information must be utilized. By choosing the weight of the shape term

proportional to the inverse of the image gradient magnitude, we employ a spatially adaptive λ_s in each iteration. As a result, for pixels on weak edges, the shape term has a higher weight than the region-based term. This also has the beneficial effect that image pixels with higher gradient (strong edges) have a stronger influence when solving for shape prior parameters. More plainly, the least squares fitting of the shape prior parameters is weighted by image gradient.

4.4. Data Acquisition

Images used in this study were acquired using a custom spectrometer based Fourier domain (FD)OCT system which has been previously described in detail in Section 2.2. Non-invasive OCT imaging was performed on seven Wistar strain albino rats. The dimension of each OCT scan was 1024 $\times$ 512 $\times$ 400 voxels covering 1.7 $\times$ 4.0 $\times$ 4.0 mm^3 and the voxel size was 1.67 $\times$ 7.80 $\times$ 10.00 μm^3. One eye on each rat underwent an axotomy procedure (severing the optic nerve); the other eye was maintained as a control in order to monitor retinal degeneration. The axotomy procedure is an accelerated model of glaucoma and causes the retinal nerve fiber layer to thin as the ganglion cells die. Each rat was imaged four times over a period of two weeks using OCT. All animal imaging procedures were compliant with animal care protocols and were performed with approval from the animal care committee. To evaluate the proposed algorithm, 80 OCT images were chosen randomly from this data set. This random image selection was restricted to the central slices of the volumes where the retinal layers were visible. OCT images from the periphery of the retinal volumes

suffered de-focus due to the crystalline lens, as also reported in other OCT studies [72], and were unusable for our experiments because the retinal layers were not clearly discernable. Figure 4-4 shows an image selected from the central area of the volume along with some images chosen from the outside of the central area.

(a)   (b)   (c)
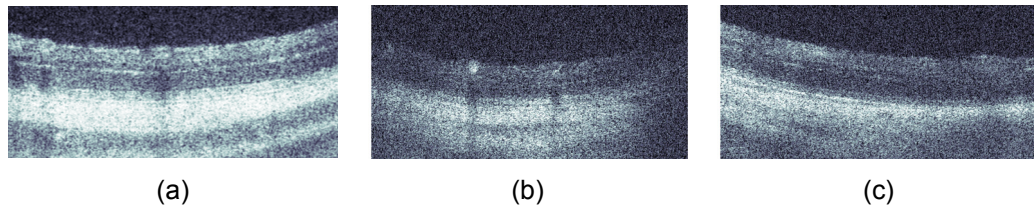
Figure 4-4. Sample of OCT images selected from (a) the central area of a volume where the retinal layers are visible, (b)-(c) outside of the central area where the retinal layers are not discernable.

4.5. Results

We applied our approach to OCT images acquired as described in Section 4.4 and for which manual segmentation was provided. We compared our segmentation approach with two other active-contour-based approaches. We refer to our method as the Active Contours without Edge with Shape constraint and contextual Weights (ACWOE–SW). The two other approaches are the classical Chan–Vese's active contours (ACWOE) and the ACWOE with shape constraint only (ACWOE–S). We assessed ACWOE–SW using three different and complementary error metrics: Dice similarity coefficient (DSC), Hausdorff Distance (HD), and absolute thickness differences. The quantitative assessment of ACWOE–SW with respect to the noise, algorithm parameters, and the initial curve was carried out in order to demonstrate the robustness of ACWOE–SW.

The computation time of the algorithm is also evaluated. An overview of the steps used for segmenting OCT data is illustrated in Figure 4-5.
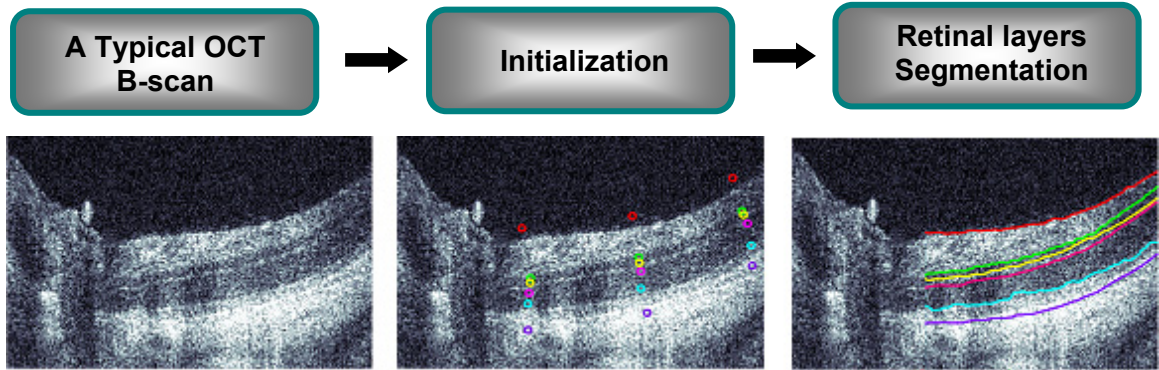
Figure 4-5. The steps used for segmenting OCT data.

4.5.1. Assessment of the Segmentation Algorithm

To qualitatively evaluate the performance of our approach, we compared the segmentation resulting from our method (ACWOE–SW) and from two other approaches (ACWOE and ACWOE–S), using the ground truth manual delineations provided by one human expert on 80 OCT images.

For each method, the parameters were chosen to give the best results. Based on our experience, the parameters were set as follows: the initial and final values for λ_I were $\lambda_I(1)=1$ and $\lambda_I(N)=0.5$ respectively. The initial and final values for λ_S were 0 and 1 respectively. λ'_R was set to 0.1×255^2 to scale the regularization term into the range of the other terms and λ''_R was set to $0.2/\Delta t$ [62]; Δt is the time step. The Chan and Vese regularization of H and δ ($\varepsilon = 1$) was used to obtain a well–defined descent direction. A maximum of 100 iterations (N) were used, which guaranteed convergence in all our experiments. For all layers, the initial curve, which is a zero level set of a SDF, was estimated

based on three points manually selected close to the interface of each layer as shown in Figure 4-5. The total number of points are three times number of layer interfaces (e.g. for the images presented in this chapter, this is 18 points per image for 6 interfaces). Every three points are used to estimate a circle. These circles are then used to create SDFs, each of which corresponds to one layer interface.

Figure 4-6 and Figure 4-7 show examples of the segmented results (with color coding) by each method for typical OCT retinal images. We can see that the ACWOE contour does not fit perfectly to the vitreo-retinal interface for most cases because there is not enough force to push the contour towards the boundary. Also, ACWOE does not show a good performance on the edges of the layers since the algorithm attempts to converge to a set of closed contours. The results with ACWOE-S, which is an extension of ACWOE by incorporating the shape prior term into the energy functional, demonstrate that ACWOE-S can delineate the vitreo-retinal interface and it does not introduce closed boundaries on the edges of the layers. However, ACWOE-S has a poor performance in the inhomogeneous regions. For example, we see a failure of this algorithm in Figure 4-7 (b). The results when applying our ACWOE-SW show that the six interfaces of retinal layers are correctly segmented specially in the presence of the intensity inhomogeneity and low contrast regions.

The segmentation results for Figure 4-6 (c) are superimposed in Figure 4-8, to appreciate the differences in segmentation quality between the three different algorithms. As shown, ACWOE–SW detects the six interfaces of the five

retinal layers properly, highlighting the performance of this method on the images with intensity inhomogeneity. Even very thin layers such as INL and OPL, which are difficult to distinguish visually, are segmented by our proposed algorithm. In contrast, ACWOE fails to segment the IPL, INL, and IS+OS layers due to the intensity inhomogeneity and low contrast of the images. ACWOE–S shows better segmentation than ACWOE, but it still has poor performance in inhomogeneous regions.

Overall, ACWOE-SW performs significantly better in comparison to two other approaches, although it may introduce minor local inaccuracy in some segmentation results. For instance, Figure 4-7 (c) shows that the contour in the location of the arrow is not completely fit to the vitreo-retinal interface because of the bright intensity artifact appearing in this location (red circle in the original image). In addition, we can see that the contours representing the (NFL+GCL+IPL)-INL and INL-OPL interfaces touch each other at the location indicated by the arrow. We contribute the lower quality of the segmentation results to the bright intensity (green circle in the original image) that connects the combined NFL+GCL+IPL layer to the OPL layer. It is worth noting that the other two approaches not only introduce similar or even worse local inaccuracy in the above-mentioned regions but also show other failures. ACWOE contour does not fit to the vitreo-retinal interface and we also see the closed contour effect at the edges of layers. ACWOE-S illustrates a poor performance in inhomogeneity regions as well.
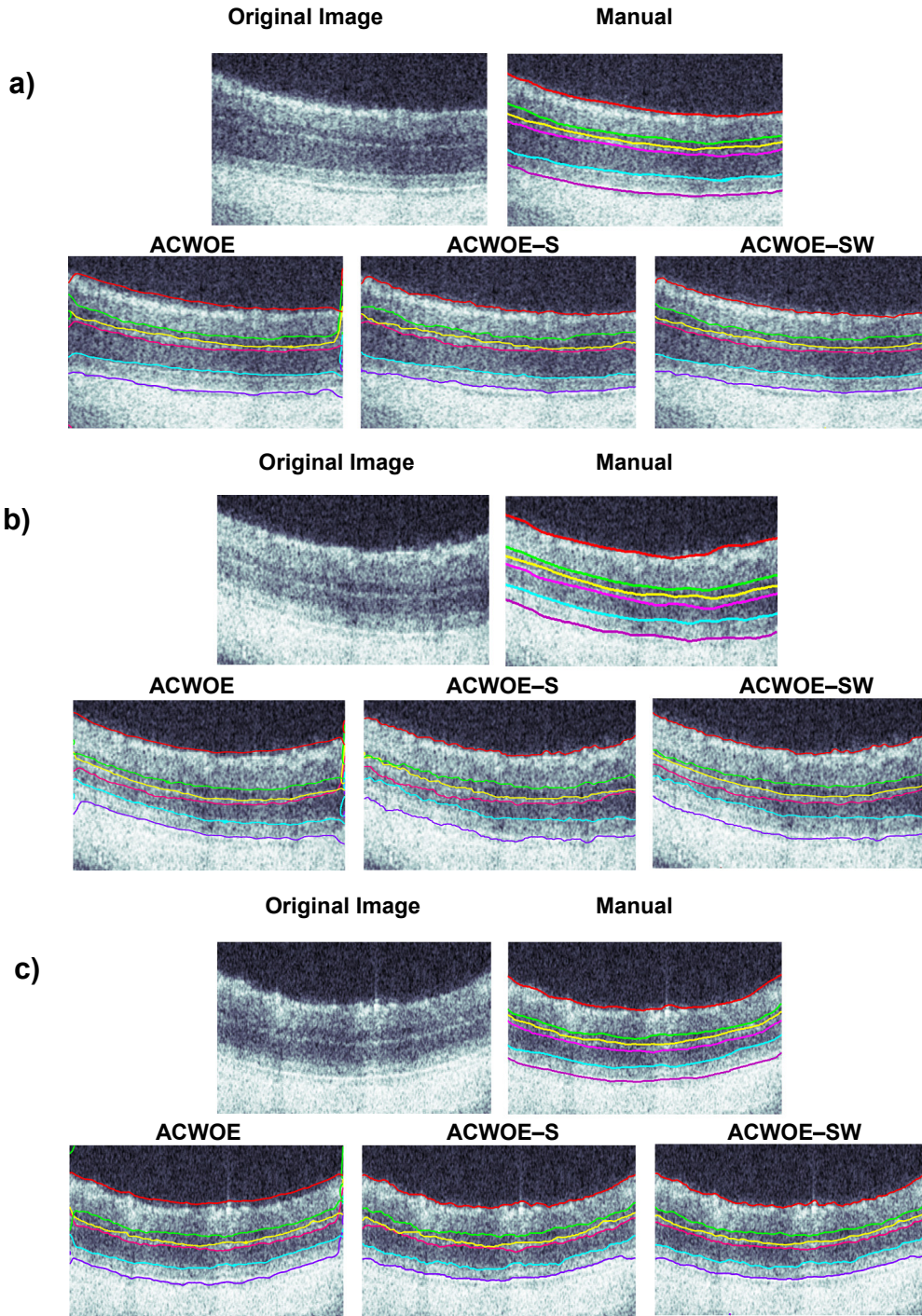
Figure 4-6. Examples of automated segmentation results shown on the OCT retinal image using different algorithms. The corresponding interfaces of retinal layers are color coded as follows: the vitreo-retinal (red), (NFL+GCL+IPL)-INL (green), INL-OPL (yellow), OPL-ONL (pink), ONL-(IS+OS) (cyan), and (IS+OS)-Retinal Pigment Epithelium (RPE) (purple).
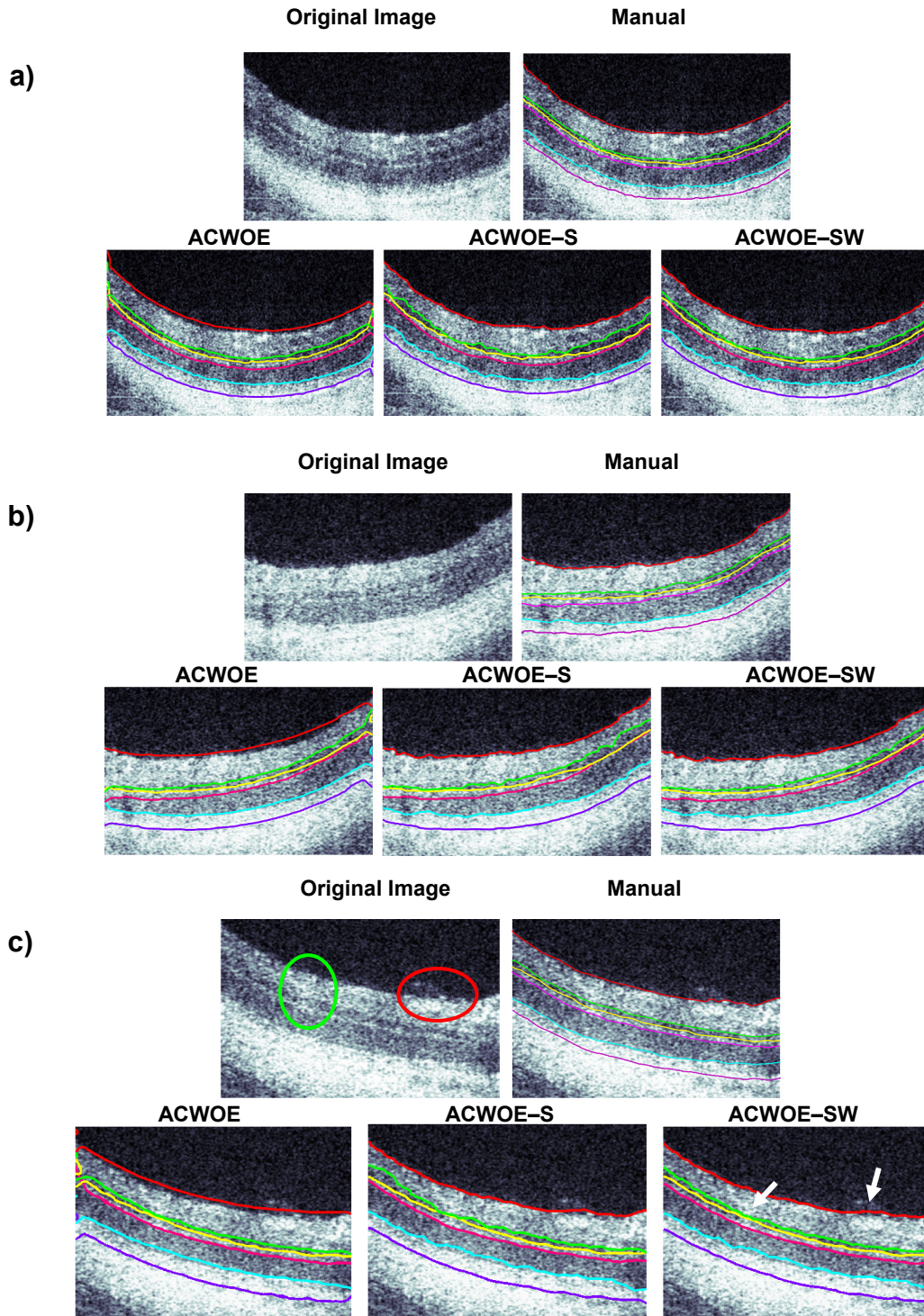
Figure 4-7. Examples of automated segmentation results shown on the OCT retinal image using different algorithms. The corresponding interfaces of retinal layers are color coded as follows: the vitreo-retinal (red), (NFL+GCL+IPL)-INL (green), INL-OPL (yellow), OPL-ONL (pink), ONL-(IS+OS) (cyan), and (IS+OS)-Retinal Pigment Epithelium (RPE) (purple). The red and green circles on the original image in Case (c) show the bright intensity artifact resulting in local inaccuracy of the three methods (highlighted by arrows for ACWOE-SW).
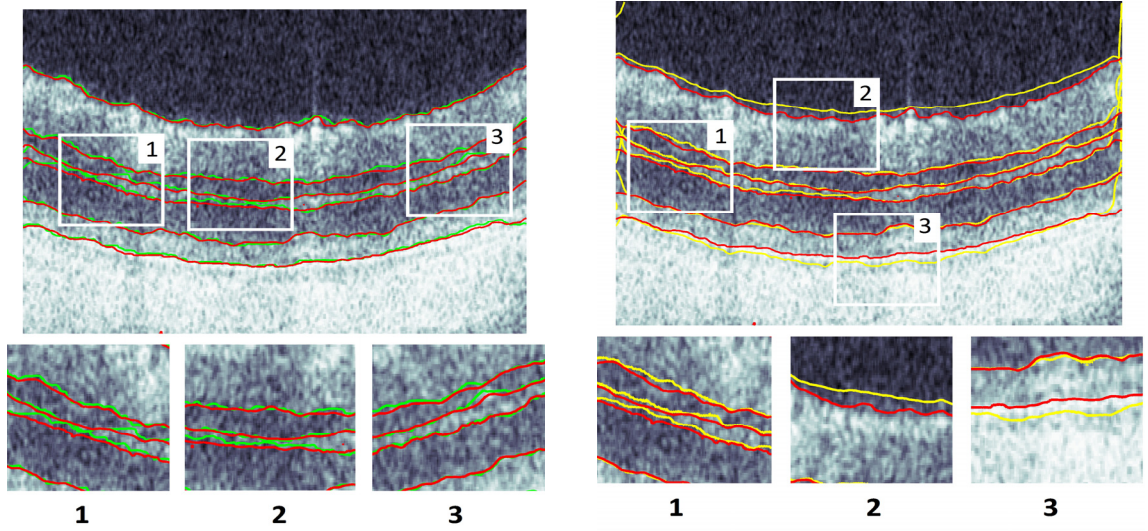
(a) ACWOE-SW (red) vs. ACWOE-S (green)   (b) ACWOE-SW (red) vs. ACWOE (yellow)

Figure 4-8. The results of the different algorithms are superimposed on each other for Case (c) in Figure 4-6 (with color coding).

To provide a quantitative evaluation of our approach, we measured the area similarity between the manual (X) and automated (Y) segmentation using DSC $\in [0,1]$ which is defined as the ratio of twice their common area to the sum of the individual areas:

$$DSC = \frac{2|X \bigcap Y|}{|X|+|Y|}.$$
(4-26)

More accurate segmentations correspond to higher DSC values. The DSC for the different retinal layers for the 80 OCT images is summarized in Figure 4-9 (a), providing a quantitative comparison of the DSC of ACWOE–SW versus ACWOE–S, and ACWOE. Our method is superior to the other approaches for all
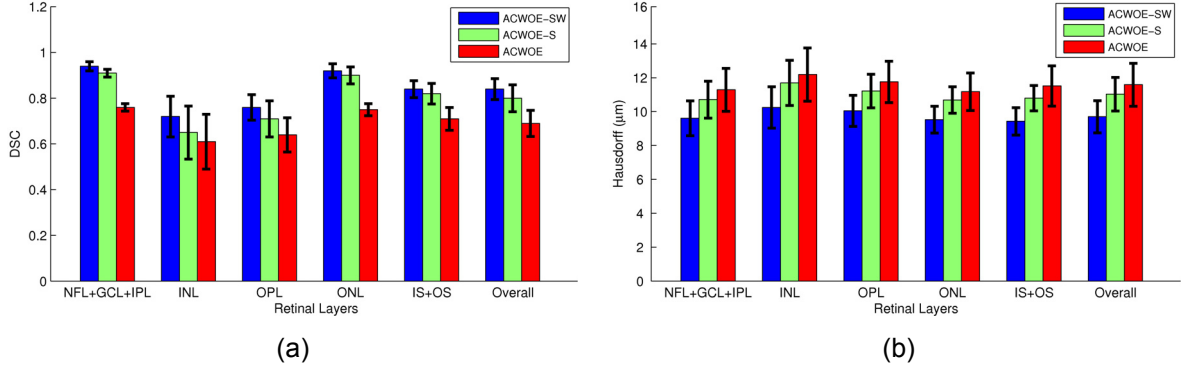
Figure 4-9. Quantitative evaluation of ACWOE-SW: (a) DSC mean and standard deviation over 80 OCT images for different retinal layers. (b) Hausdorff distance mean and standard deviation (µm) over 80 OCT images for different retinal layers.

the examined layers. Specifically for NFL+GCL+IPL, the DSC of our algorithm is 0.94 resulting in $\sim 0.06\%$ error (a tolerable error for monitoring degeneration of retinal layers).

In addition, the mean Hausdorff distance defined in (4-27) was computed for the segmented and ground–truth boundaries of each retinal layer over 80 OCT images. Figure 4-9 (b) summarizes the computed maximal boundary mismatch (HD) for our method, ACWOE–SW, versus two other methods, ACWOE–S and ACWOE.

$$HD(A,B) = \max(\max_{a \in A}\{\min_{b \in B}\{\| a - b \|\}\}, \max_{b \in B}\{\min_{a \in A}\{\| a - b \|\}\}), \qquad (4\text{-}27)$$

where A and B are sets of points extracted form the segmented and ground truth boundaries respectively. According to Figure 4-9 (b), ACWOE–SW results in the smallest average Hausdorf distance for all layers. The average HD achieved is $9.77\,\mu m$. Considering the typical total retinal thickness of $190\,\mu m$ [4], the error of our algorithm is 5.1% in total.

Finally, the mean thickness of retinal layers was computed for all images using three algorithms, ACWOE–SW, ACWOE–S, and ACWOE. The layer thicknesses from the manual segmentation was used as a gold standard. Table 4-1 and Table 4-2 show the absolute and relative thickness differences, respectively. As shown, the smallest thickness difference for our method, ACWOE–S, and ACWOE were achieved for ONL layer ($2.54 \pm 1.16 \mu m$ for our approach, $2.84 \pm 1.23 \mu m$ for ACWOE–S and $3.49 \pm 1.19 \mu m$ for ACWOE). In contrast, the maximum thickness difference for our approach occurred in NFL+GCL+IPL layer ($3.76 \pm 1.47 \mu m$) which is acceptable considering the total thickness of $61.76 \mu m$ for this layer. Note that the thickness difference averaged over all the layers for our method ($3.15 \pm 1.37 \mu m$) is less than the two other methods.

Table 4-1. Mean and standard deviation of thickness differences calculated using the results of different methods (ACWOE–SW, ACWOE–S, and ACWOE) and the ground truth manual segmentation, over 80 OCT images for retinal layers. Absolute thickness differences (*μm*) along with the average thickness (*μm*) of each layer are reported.

Layers	Average thickness (*μm*)	Absolute thickness differences (*μm*) (Mean ± SD)		
		ACWOE-SW	ACWOE-S	ACWOE
NFL+GCL +IPL	61.76	3.76 ± 1.47	4.12 ± 1.70	5.90 ± 2.37
INL	17.74	2.94 ± 1.11	3.30 ± 1.09	4.18 ± 1.77
OPL	21.46	3.06 ± 1.38	3.33 ± 1.77	3.84 ± 1.36
ONL	52.05	2.54 ± 1.16	2.84 ± 1.23	3.49 ± 1.19
IS+OS	35.76	3.43 ± 1.77	4.52 ± 2.72	5.06 ± 2.66
Overall	188.77	**3.15 ± 1.37**	3.62 ± 1.70	4.49 ± 1.87

Table 4-2. Mean and standard deviation of thickness differences calculated using the results of different methods (ACWOE–SW, ACWOE–S, and ACWOE) and the ground truth manual segmentation, over 80 OCT images for retinal layers. Relative thickness differences along with the average thickness (*µm*) of each layer are reported.

Layers	Average thickness (*µm*)	Relative thickness differences (Mean ± SD)		
		ACWOE-SW	ACWOE-S	ACWOE
NFL+GCL +IPL	61.76	0.06 $\pm$ 0.02	0.07 $\pm$ 0.03	0.10 $\pm$ 0.04
INL	17.74	0.16 $\pm$ 0.06	0.18 $\pm$ 0.06	0.23 $\pm$ 0.10
OPL	21.46	0.14 $\pm$ 0.06	0.16 $\pm$ 0.08	0.18 $\pm$ 0.06
ONL	52.05	0.04 $\pm$ 0.02	0.05 $\pm$ 0.02	0.07 $\pm$ 0.02
IS+OS	35.76	0.09 $\pm$ 0.05	0.13 $\pm$ 0.08	0.14 $\pm$ 0.07
Overall	188.77	**0.10 $\pm$ 0.04**	0.12 $\pm$ 0.06	0.14 $\pm$ 0.06

4.5.2. Noise Tolerance

In order to evaluate the robustness of our algorithm to noise, controlled synthetic retinal OCT-like images were created with known ground truth segmentation but corrupted with varying degrees of noise. OCT images are contaminated with speckle noise which results from constructive and destructive interferences of backscattered waves and appears as a random granular pattern [35], [73], [74]. Applying a logarithmic transform to the image converts the multiplicative speckle noise into additive white Gaussian noise [38]-[41], [75]. To create the synthetic OCT-like images, after applying a logarithmic transform, the ground truth segmentation was corrupted by additive white Gaussian noise with probability density function $N(0, \sigma^2)$, where the noise variance, σ^2, was changed in the range of $[0 \ 0.8] \times 255^2$. Synthetic images were constructed with and without artifacts to simulate typical features of OCT images. Examples of these synthetic images are presented in Figure 4-10. The dark blood vessel attenuation (intensity

(a)   (b)
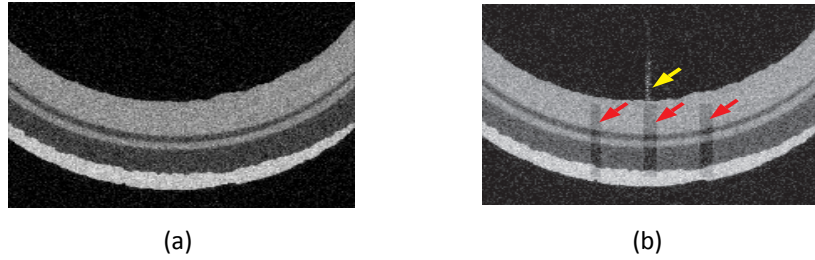
Figure 4-10. Synthetic retinal OCT-like images (for $\sigma^2=0.05\times255^2$): (a) without artifact, (b) with intensity inhomogeneity (red arrows) and bright saturation (yellow arrow) artifacts.

(a)   (b)
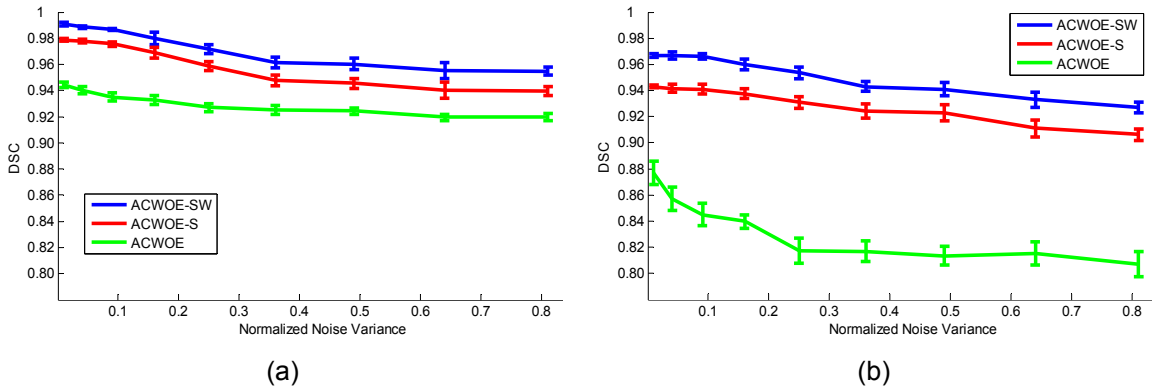
Figure 4-11. Dice similarity coefficient for different noise levels in the synthetic data, (a) without artifacts, (b) with artifacts.

inhomogeneity) and bright saturation artifact were considered as predominant sources of artifacts affecting the OCT images. The latter is due to high back scattering intensity from the vitreo–retinal interface, while the intensity inhomogeneity, as a general artifact in OCT retina images [42]-[44], results from the absorption of light by the blood vessels in the retina. As shown in Figure 4-11, the DSC performance results reveal that adding a shape constraint to the energy functional makes the algorithm more accurate than standard ACWOE, while remaining robust in the presence of noise. Adding artifacts to the synthetic images decreases the DSC for all three methods while ACWOE–SW still exhibits the highest accuracy.

61

4.5.3. Parameters and Initialization Perturbations

The objective of this section is to investigate the sensitivity of the algorithm with respect to the parameters λ_I, λ_S, and λ'_R as well as the initial curve. Recalling from Section 4.1, the energy functional is a weighted summation of three energy terms with different weights. Also, a contextual scheme was used to balance the weight of different terms. The parameters λ_I, λ_S, and λ'_R were selected empirically (λ''_R was set to $0.2/\Delta t$, where Δt is the time step).

As λ_I and λ_S are two different functions of iteration number n, we related λ_I to λ_S using their initial values by $\lambda_S(1) = max(0, 1 - \lambda_I(1))$. Then, we varied the value of the $\lambda_I(1)$ from 0.8 to 1.2 (i.e. $\lambda_I(1) \pm 20\%$) and applied the algorithm on the same data set of 80 OCT images. To assess the sensitivity of the algorithm with respect to change in parameters, we compared our method's segmentation results with the corresponding ground truth manual segmentation using DSC and HD. As we can see in Figure 4-12(a), changing $\lambda_I(1)$ by $\pm20\%$ resulted in an average change of $\pm0.55\%$ in DSC, specifically $\pm0.41\%$ for the NFL+GCL+IPL layer. In addition, the same change in $\lambda_I(1)$ brought about a change of $\pm1.7\%$ for HD averaged over all layers and $\pm1.30\%$ for the NFL+GCL+IPL as illustrated in Figure 4-12 (b). The results reveal the robustness of our approach with respect to the change in these parameters.

(a)   (b)
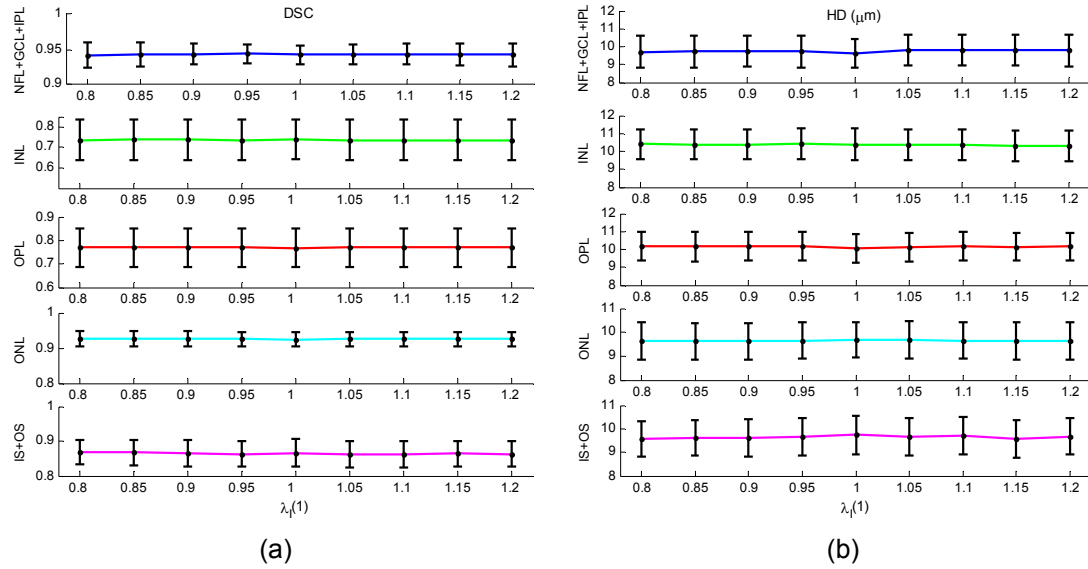
Figure 4-12. Sensitivity of the algorithm to the contextual parameters defined in (4-25). (a) DSC mean and standard deviation over 80 OCT images for different $\lambda_I(1)$. (b) Hausdorff distance mean and standard deviation over 80 OCT images for different $\lambda_I(1)$.

(a)   (b)

Figure 4-13. Sensitivity of the algorithm to the regularization parameter λ'_R. (a) DSC mean and standard deviation over 80 OCT images for different values of λ'_R. (b) Hausdorff distance mean and standard deviation over 80 OCT images for different values of λ'_R.

To investigate the effect of changes in parameter λ'_R on the algorithm performance, we applied the algorithm on the data set of 80 images with different values of this parameter, while holding the other parameters fixed. The values

selected for λ'_R were $[0, 0.01, 0.05, 0.1, 0.2, 0.5, 1, 2] \times 255^2$. In each case, the algorithm segmentation results were compared with the corresponding ground truth manual segmentation using DSC and HD. The results of this assessment are shown in Figure 4-13, suggesting that with the goal of achieving a correct segmentation of retinal layers, the value selected for parameter λ'_R in this work is appropriate.

We performed a similar experiment for assessing the algorithm sensitivity to the initialization using 80 OCT images. Retinal layers have different thicknesses; therefore, the initial curve radius was changed according to the related retinal layer thickness. In particular, the radius was varied by up to 30% of the corresponding layer thickness. Considering the structure of the retinal layers and the average thickness reported in Table 4-1, varying the initial contour by more than $\sim 30\%$ of the corresponding layer thickness is not feasible because doing so would potentially result in the initial contour for a layer falling between the boundaries of the adjacent layers, resulting in segmenting the wrong interfaces.

The results of the algorithm sensitivity to the user initialization are presented in Figure 4-14 for DSC and HD metrics. Overall, the algorithm segments the retinal layers with an average change of 10.54% and 2.92% for DSC and HD, respectively. The sensitivity to the initialization for the other two methods was similarly assessed, resulting in an average DSC of 12.94% and 17.10% and an average HD of 3.78% and 4.03% for ACWOE–SW and ACWOE, respectively.

DSC   HD (μm)

(a)   (b)
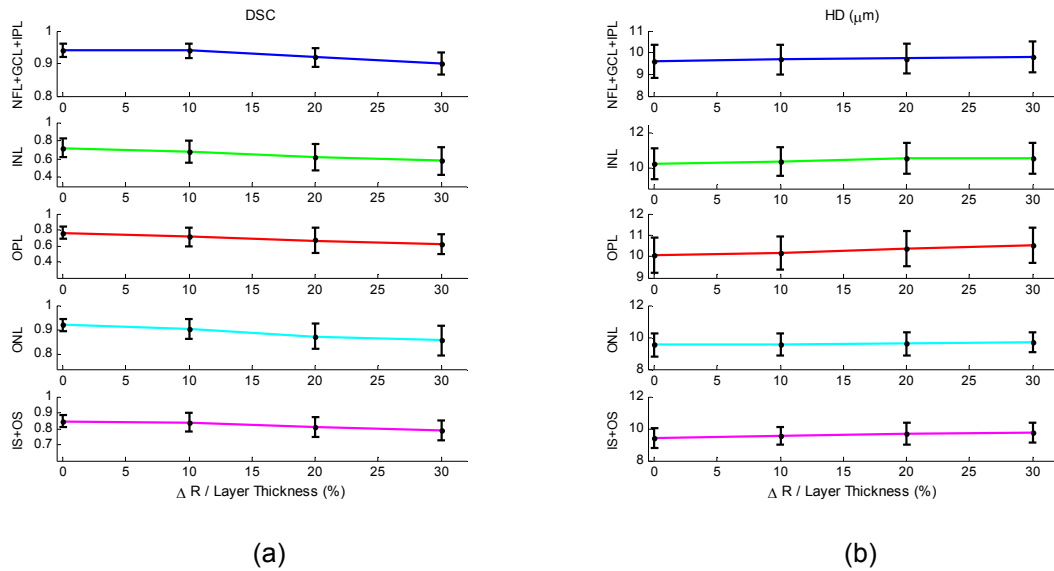
Figure 4-14. Change in DSC and HD as the initial contour is perturbed. (a) DSC mean and standard deviation over 80 OCT images for different initial curves. (b) Hausdorff distance me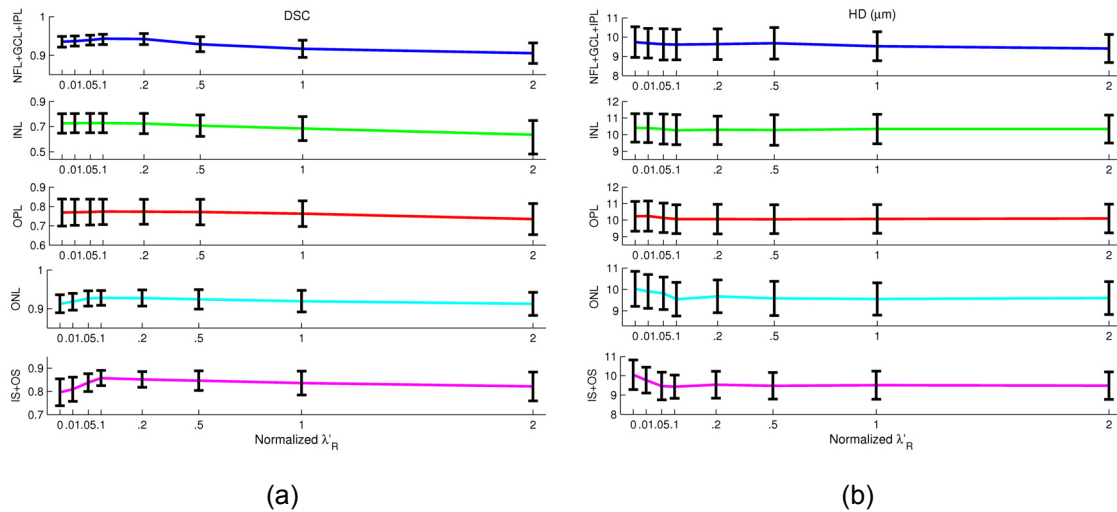an and standard deviation over 80 OCT images for different initial curves. ΔR is the change in the radius of initial contour in pixels.

4.5.4. Computation Time

The processing time for the different methods was also assessed in this study. Table 4-3 reports the average (± standard deviation) computation time of different methods applied to the set of 80 OCT images using a personal computer (Microsoft Windows 7 Professional 64-bit edition, Intel Core i7, CPU 2.67 GHz, 6.00 GB of RAM). The OCT image size was 1024 pixels axially and 512 pixels laterally. As a pre-processing step, each image was cropped axially to the region of interest (600 × 512 pixels) that included the retina.

Table 4-3. The average (± standard deviation) processing time of different methods over 80 OCT images.

Method	Average (± SD) Time (s)	Time per iteration (s)
ACWOE-SW	95 ± 0.28	0.95 ± 0.03
ACWOE-S	94 ± 0.16	0.94 ± 0.03
ACWOE	58 ± 0.15	0.58 ± 0.02

The average (± standard deviation) of the mean computation time per iteration for ACWOE–SW, ACWOE–S, and ACWOE is 0.95 ± 0.03 s, 0.94 ± 0.03 s, and 0.58 ± 0.02 s, respectively, calculated over the set of 80 images. For each method, the DSC was calculated at each iteration. Figure 4-15 illustrates the average DSC over 80 images as a function of iteration. A maximum of 100 iterations is sufficient for convergence of the algorithms; additional iterations do not change the calculated segmentation accuracy given by DSC. According to
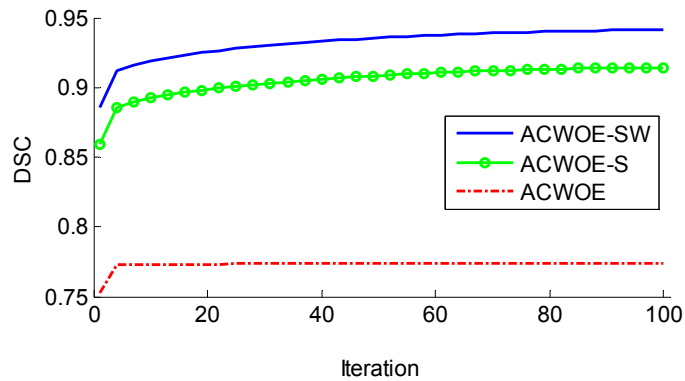
Figure 4-15. The average DSC calculated over 80 OCT images for each iteration. Since the standard deviation of DSC is very small (less than 0.005) in comparison to the mean value, it is not shown in the plot.

the results, ACWOE–SW is fast enough for our practical purposes and provides more accurate segmentation. In addition, our method can be optimized to run faster using algorithm optimization approaches such as the multi-grid methods.

4.6. Chapter Summary and Conclusions

In this chapter, we discussed a novel iterative algorithm to segment OCT images of retinal layers using a multi-phase framework with a circular shape prior. The methodology and numerical implementation of our algorithm were described in detail. In order to evaluate the segmentation method, automated

segmentation results were compared with the ground truth manual segmentation as well as the results of two other active-contour-based approaches.

We have demonstrated that our approach is able to accurately segment all of the intra-retinal layers, even when the small size and similar texture make them difficult to distinguish visually. Our approach also shows that the inclusion of a shape prior constraint improves performance on regions with intensity inhomogeneity. We also introduced a contextual scheme to balance the weight of different terms in the energy functional, which makes the algorithm more robust when the image information is not sufficient to accurately detect the layers.

Our method is a region-based segmentation approach combining the intensity information and the implicit use of edge information, through the shape term, to improve the final segmentation accuracy. The proposed method, ACWOE–SW, was shown to be more accurate in the presence of noise than the other region-based active contours methods. The sensitivity of ACWOE–SW with respect to changes in parameters and the initial curve was also investigated, revealing the robustness of the ACWOE–SW with respect to these changes. Assessing the computation time of the algorithm, it was shown that ACWOE–SW is fast enough for our practical purposes.

5. LONGITUDINAL STUDY OF RETINAL DEGENERATION IN RAT

In this chapter, we investigate the quantitative measurement of longitudinal retinal thickness in rat retinal degeneration using our intra-retinal layer segmentation algorithm, described in Chapter 4. Volumetric OCT images of the retina in a time course study were segmented using the segmentation algorithm. Then, thickness of the NGI (NFL+GCL+IPL) layer was quantified across the surface of the retina for multiple volume segmentations. The resulting retinal thickness maps over time were used to quantify the thinning of the NGI during injury.

5.1. Data

The images used in this work were acquired using a custom spectrometer based Fourier domain (FD) OCT, described in Section 2.2. Volumetric OCT imaging was performed over 14 days post-axotomy (Days 3, 7, 10, and 14) according to the image acquisition procedure discussed previously in Section 2.2. The right eye on each rat underwent an axotomy procedure (severing the optic nerve); the contralateral eye was maintained as a control in order to monitor retinal degeneration. The axotomy procedure is an accelerated model of glaucoma and causes an acute injury that induces degeneration over the whole retina. Following the axotomy, the death of the ganglion cells and nerve fibers results in thickness changes in the corresponding retinal layers. All animal

imaging procedures were compliant with animal care protocols and were performed with approval from the animal care committee.

5.2. Methods

The rat retina volumes were pre-processed for axial motion correction, and cropped to exclude the Optic Nerve Head (ONH) and the edges of the volume. The OCT volumetric images were acquired from the peripapillary region near the ONH, where the retinal layers disappeared as illustrated in Figure 5-1 (b). Therefore, to segment these images, we have cut the region inside of the ONH and performed the segmentation on the rest of the volume. In addition, OCT images from the periphery (the edges) of the volumes suffered de-focus due to the crystalline lens, as also reported in other OCT studies [72], and were unusable for our experiments because the retinal layers were not clearly discernable. The retinal layers were segmented in each OCT B-scan using ACWOE-SW. The algorithm segmented five intra-retinal layers simultaneously, but only the NGI layer was considered for this study. An example of the segmented results for typical OCT retinal images is shown in Figure 5-1 (c). The volume segmentation is defined as surfaces bounding the NGI in 3D space. Following the segmentation, the thickness of the retina layers was calculated in 3D using the Laplacian Streamline Correspondence Thickness (LSCT) method [30], [76].
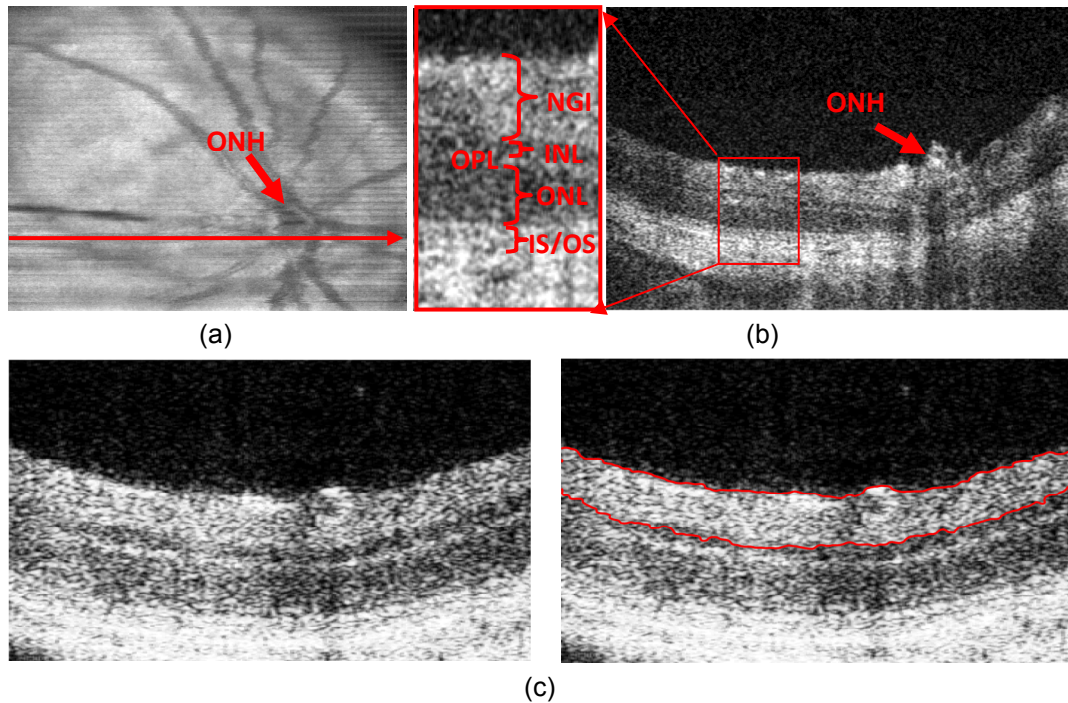
Figure 5-1. (a) An *en face* image centered at ONH, (b) a typical OCT B-scan extracted from the position of red arrow. Retinal layers disappear in ONH region. (c) Results of automatic segmentation of NGI layers on OCT images (right), along with the original image (left).

5.3. Results

The 2D colour coded NGI thickness maps from Days 3, 7, 10, and 14 post-axotomy are shown in Figure 5-2 overlaid on their corresponding reconstructed *en face* images.

The change in thickness of the NGI as a function of distance from the ONH and time can be extracted from the thickness maps in Figure 5-2. The mean and standard deviation of the thickness values for the pixels lying between each two consecutive circles and falling within the strip (i.e. the common sector between two consecutive circles and the strip) were then calculated. The strip was manually selected by the user for each volume due to the realignment

70
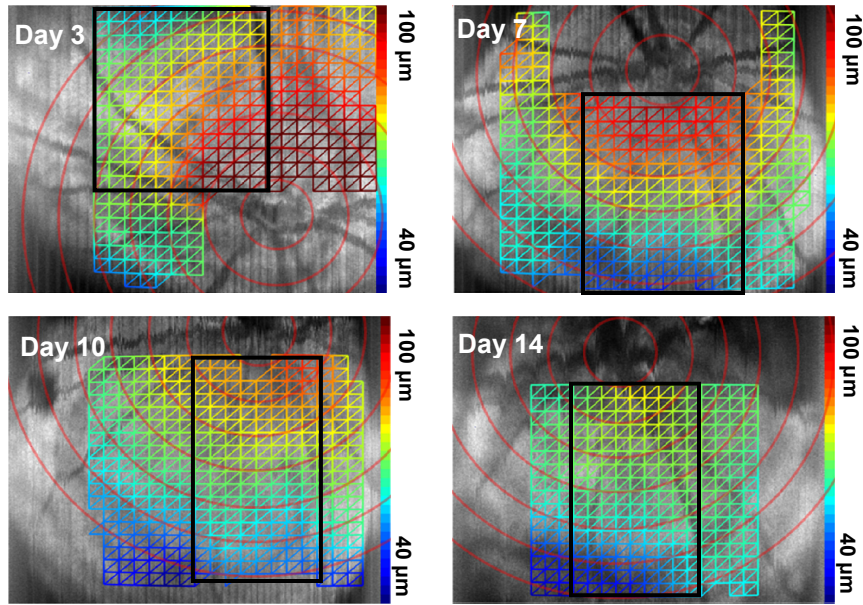
Figure 5-2. Summary of 2D colour code thickness maps of the combined NGI layers are superimposed on the summed voxel projection of retinal volumes acquired in a time course study of retinal degeneration in a rat following optic nerve transection [30].

Issues. Since the OCT system only provides a two dimensional depth profile of the retina in real time, alignment of the OCT system to the same point on the retina (e.g. ONH) in a longitudinal study is challenging. Alignment of the OCT scan area to the ONH is performed based on the fly-through images observed in real time during volumetric acquisition. Another problem is that the orientation of the eye is different between imaging sessions because the rats roll their eyes when anesthetized.

Figure 5-3 presents the NGI thickness results at different distances from ONH for both the control and axatomy eyes. In the case of axatomy, the thickness changes are depicted at different time points. Overall, the thickness reduces gradually as the distance from ONH increases. Also, selecting a specific distance from ONH, the thickness plots from the axotomy eye show a decreasing

trend in NGI thickness in successive days. As a case in point, at ~1500 *µm* from

ONH, the thickness changes from 78 *µm* (day3) to 66 *µm* (day 14).
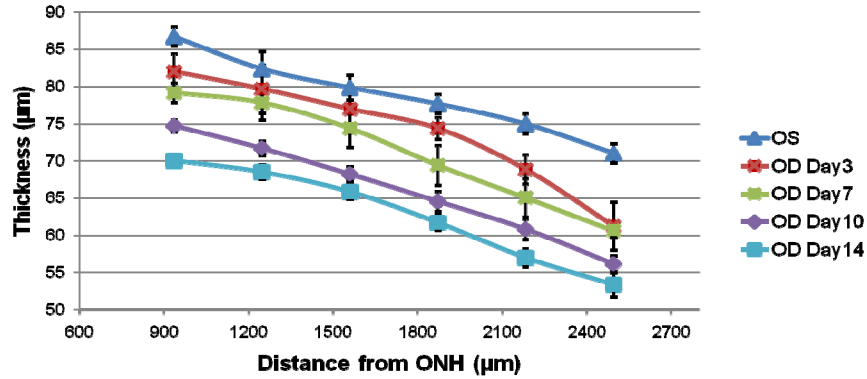
Figure 5-3. Average thickness of the NGI as a function of distance from the ONH. OS: left eye, control; OD: right eye with optic nerve transaction [30].

5.4. Chapter Summary and Conclusions

We demonstrated quantitative measurement of the longitudinal thinning of

the combined NGI in a rat that had undergone optic nerve transection. Using the

active-contour algorithm proposed in Chapter 4, the layers of the rodent retina in

both the control and axatomy eyes were segmented, and the NGI complex

thickness over time was quantified by the Laplacian streamlines adopted from a

previous publication [30], [76]. Automated segmentation, avoiding manual inter-

and intra-rater variability, holds the potential to reduce the time and effort

required to delineate the retinal layers and also to provide repeatable,

quantitative results. The combination of our segmentation algorithms and

thickness measurements of the retinal cell layers from FD OCT volumes provides

a powerful computational anatomical tool for vision scientist. While we focus on

the quantitative measurement of the NGI layers in a model of acute retinal injury

in this chapter, the proposed computational pipeline can be readily extended to investigate rodent models of retinal degenerative diseases affecting other retinal cell layers, such as the outer nuclear layer.

6. SUMMARY AND CONCLUSIONS

This thesis introduced a novel active contour based segmentation approach and evaluated its performance when applied to delineate the intra-retinal layers from OCT images. Quantitative measurement of the longitudinal retinal thickness in rat retinal degeneration was also demonstrated using our intra-retinal layer segmentation algorithm as a pre-clinical application of our proposed method.

6.1. Summary

We reviewed the state of the art OCT as a prominent ophthalmic diagnostic technique. We adapted OCT for imaging rodent eyes in order to complement medical research and study retinal degeneration. As discussed, OCT images of rat eye are of relatively low quality and highly corrupted by speckle noise and suffer from intensity inhomogeneities and bright saturation artifact, presenting challenges for retinal layer segmentation algorithms. We proposed a novel iterative algorithm to segment OCT images of retinal layers to address these problems. Our approach is able to segment all of the intra-retinal layers simultaneously due to the multi-phase property of the algorithm. Each region is represented by estimating its corresponding characteristic function. The inclusion of a shape prior constraint improves performance on regions with intensity inhomogeneity. The shape prior was concentric circles based on expert anatomical knowledge of the retinal layers, avoiding the need for training. The

proposed shape prior is a soft constraint rather than a hard one and does not hurt the segmentation results when the layers are less likely to resemble the assumed shape prior.

We also employed temporally and spatially adaptive weights to balance the weight of different terms in the energy functional. The contextual scheme provides an intricate balance between image and prior, which makes the algorithm more robust when the image information is not sufficient to accurately detect the layers.

Our method is a region-based segmentation approach combining the intensity information and the implicit use of edge information, through the shape term, to improve the final segmentation accuracy. Our preliminary comparison to active contour segmentation approaches, which rely solely on image intensity [31] or edge information [57], revealed that these methods fail to properly segment the retinal layers especially INL, OPL, and IS+OS. We also found that edge-based active contours were much more sensitive to initialization and noise than the region-based approaches. The proposed method, ACWOE–SW, was shown to be more accurate in the presence of noise than the other region-based active contours methods.

The sensitivity of the proposed algorithm with respect to changes in parameters and the initial curve was also investigated, revealing the robustness of the ACWOE–SW with respect to these changes. The robustness and accuracy of the algorithm was also demonstrated through application to both synthetic data and retinal images from rats. The segmentation results were validated by

comparing them with the ground truth manual expert delineations using Dice similarity coefficient, Hausdorff Distance, and absolute thickness differences. The experimental results showed that the algorithm detects the desired retinal layers, and achieves an acceptable level of accuracy.

The developed segmentation approach is based on the level set framework which naturally handles topological changes and extends easily to higher dimensions. The circular shape prior can be also extended to a spherical or a more general shape, such as an ellipsoid, by incorporating the third dimension in the relevant equations. The 3-D model of our proposed method is obtained by generalizing the formulation given in Section 4.1. Doing so, one may extend our work to 3-D active surface and segment the volumetric OCT images. The major issue is the high computational cost, which is a function of the image resolution and can be tackled by incorporating accelerating methods, such as the fast marching methods [77]-[79] or narrowband techniques [80], [81].

Finally, the proposed segmentation approach was applied to illustrate the longitudinal study on a rat that had undergone optic nerve transection. The layers of the rodent retina were segmented using ACWOE-SW, and the thickness of NGI over time was measured. While the NGI thickness in both the axotomy and contralateral eyes decreases by increasing distance from the optic nerve head, the NGI complex thickness in the affected eye decreases in successive days as well. Our segmentation algorithm provides a powerful computational anatomical tool for vision scientists to investigate retinal degenerative diseases affecting

other retinal cell layers by extraction of individual layer properties (e.g. thickness).

6.2. Future work

The segmentation method developed in this study has a number of potential applications and future directions. Although demonstrated here for the segmentation of the retinal layers in OCT images, the contributions of spatially and temporally adaptive parameters discussed in this thesis are not restricted to rat OCT applications specifically, or even OCT in general. These contributions can benefit other applications and assist in improving the accuracy and convergence of other methods as well. Further, we believe the simultaneous segmentation of multiple layers may be generalized to address segmentation of multiple objects where there are more elaborate spatial relationships between objects, e.g. one is a subset of or is adjacent to the other.

Future improvements to our algorithm include making it more independent of the user by automating the setting of the parameters based on machine learning methods [82]-[88] or based on image cues [89], [64]. An additional direction for improvement is to develop an automatic initialization method which results in initial contours close to the surfaces of retinal layers, guaranteeing the convergence of the algorithm to desirable local minima (i.e. segmenting the interface of retinal layers). However, an alternative approach is to eliminate the dependency on the position of the initial curve based on investigating convex formulations with globally optimal solutions [90]-[93].

Application of the algorithm on a larger database of rats suffering from a variety of retinal diseases is also of interest and is left for future work. The ACWOE–SW can be also extended to human OCT images. Because the human eye is a significantly better optical system than that of rodents, human retinal OCT images are of higher quality than the rodent retinal images presented here. Migrating our ACWOE–SW method to segment human retinal images will require customizing the shape prior to incorporate the foveal pit and/or the cup shape of ONH, but otherwise is anticipated to provide similar segmentation results. The discontinuity of the retinal layers due to ONH and fovea constitutes additional issues, which can be addressed by customizing the weights of energy terms and applying the algorithm in two steps. In the first step, the vitreo-retinal interface would be segmented. Then by considering the location of the vitreo-retinal interface, the rest of the layers can be segmented. We would also need to find the optimal weight for each term in energy functional as well as to define different weighting scheme for different layers in order to segment the cup shape of ONH in human data.

REFERENCE LIST

[1]   C. A. Puliafito, "Imaging of macular diseases with optical coherence tomography," *Ophthalmology*, vol. 102, 1995, pp. 217-229.

[2]   M.R. Hee, J.A. Izatt, E.A. Swanson, D. Huang, J.S. Schuman, C.P. Lin, C.A. Puliafito, and J.G. Fujimoto, "Optical Coherence Tomography of the Human Retina," *Arch Ophthalmol.*, vol. 113, 1995, pp. 325-332.

[3]   Q. Li, A.M. Timmers, K. Hunter, C. Gonzalez-Pola, A.S. Lewin, D.H. Reitze, and W.W. Hauswirth, "Noninvasive imaging by optical coherence tomography to monitor retinal degeneration in the mouse.," *Investigative Ophthalmology & Visual Science*, vol. 42, Nov. 2001, pp. 2981-2989.

[4]   V.J. Srinivasan, T.H. Ko, M. Wojtkowski, M. Carvalho, A. Clermont, S.-E. Bursell, Q.H. Song, J. Lem, J.S. Duker, J.S. Schuman, and J.G. Fujimoto, "Noninvasive volumetric imaging and morphometry of the rodent retina with high-speed, ultrahigh-resolution optical coherence tomography.," *Investigative Ophthalmology & Visual Science*, vol. 47, Dec. 2006, pp. 5522-5528.

[5]   M. Ruggeri, H. Wehbe, S. Jiao, G. Gregori, M.E. Jockovich, A. Hackam, Y. Duan, and C.A. Puliafito, "In vivo three-dimensional high-resolution imaging of rodent retina with spectral-domain optical coherence tomography.," *Investigative Ophthalmology & Visual Science,* vol. 48, Apr. 2007, pp. 1808-1814.

[6]   A. Walsh and S. Sadda, "Optical Coherence Tomography in the Diagnosis of Retinal Vascular Disease," A. M. Joussen, T. W. Gardner, B. Kirchhof, and S. J. Ryan, Eds. *Springer Berlin Heidelberg*, 2007, pp. 205-227.

[7]   J. Xu, L.L. Molday, R.S. Molday, and M.V. Sarunic, "In vivo imaging of the mouse model of X-linked juvenile retinoschisis with fourier domain optical coherence tomography.," *Investigative Ophthalmology & Visual Science*, vol. 50, Jun. 2009, pp. 2989-2993.

[8]   S. Resnikoff, D. Pascolini, D. Etya, I. Kocur, R. Pararajasegaram, G.P. Pokharel, and S.P. Mariotti, "Policy and Practice Global data on visual impairment in the year 2002," *Bulletin of the World Health Organization*, vol. 82, 2004, pp. 844-851.

[9]   L. Leonard A Daniel M., Albert, *Ocular Disease: Mechanisms and Management*, Saunders, 2010.

[10]   M.K. Garvin, "Automated 3-D segmentation and analysis of retinal optical coherence tomography images," PhD Thesis, The University of Iowa, 2008.

[11]   L.A. Remington, *Clinical Anatomy of the Visual System*, Elsevier Inc., 2005.

[12]   N. Hossein-Javaheri, "Non-Invasive Retinal Imaging in Mice with Fluorescent Scanning Laser Ophthalmoscopy and Fourier Domain Optical Coherence Tomography," Master's Thesis, Simon Fraser University, 2010.

[13]   L.M. Chalupa and R.W. Williams, *Eye, Retina, and Visual System of the Mouse*, MIT Press, 2008.

[14]   A. Yazdanpanah, G. Hamarneh, B. Smith, and M. Sarunic, "Intra-retinal layer segmentation in optical coherence tomography using an active contour approach.," *Medical Image Computing and Computer-Assisted Intervention : MICCAI*, 2009, pp. 649-656.

[15]   D.C. Fernandez, H.M. Salinas, and C.A. Puliafito, "Automated detection of retinal layer structures on optical coherence tomography images," *Opt. Express*, vol. 13, 2005, pp. 200-216.

[16]   D.C. Fernández, "Delineating fluid-filled region boundaries in optical coherence tomography images of the retina.," *IEEE Transactions on Medical Imaging*, vol. 24, Aug. 2005, pp. 929-945.

[17]   A.M. Bagci, M. Shahidi, R. Ansari, M. Blair, N.P. Blair, and R. Zelkha, "Thickness profiles of retinal layers by optical coherence tomography image segmentation.," *American Journal of Ophthalmology*, vol. 146, Nov. 2008, pp. 679-687.

[18]   D. Koozekanani, K. Boyer, and C. Roberts, "Retinal thickness measurements from optical coherence tomography using a Markov boundary model," *IEEE Transactions on Medical Imaging*, vol. 20, pp. 900-916.

[19]   R.J. Zawadzki, A.R. Fuller, D.F. Wiley, B. Hamann, S.S. Choi, and J.S. Werner, "Adaptation of a support vector machine algorithm for segmentation and visualization of retinal structures in volumetric optical coherence tomography data sets," *Journal of Biomedical Optics*, vol. 12, 2007, pp. 041206.

[20] A. Fuller, R. Zawadzki, S. Choi, D. Wiley, J. Werner, and B. Hamann, "Segmentation of three-dimensional retinal image data.," *IEEE Transactions on Visualization and Computer Graphics*, vol. 13, 2007, pp. 1719 - 1726.

[21] M.K. Garvin, M.D. Abramoff, R. Kardon, S.R. Russell, X. Wu, and M. Sonka, "Intraretinal layer segmentation of macular optical coherence tomography images using optimal 3-D graph search.," *IEEE Transactions on Medical Imaging*, vol. 27, Oct. 2008, pp. 1495-505.

[22] M. Haeker, M.D. Abràmoff, R. Kardon, and M. Sonka, "Segmentation of the surfaces of the retinal layer from OCT images," *in Proceedings of the 9th International Conference on Medical Image Computing and Computer-Assisted Intervention (MICCAI)*, 2006, pp. 800-807.

[23] M. Haeker, M. Sonka, R. Kardon, V.A. Shah, X. Wu, and M.D. Abramoff, "Automated segmentation of intraretinal layers from macular optical coherence tomography images," *in Proceedings of SPIE Medical Imaging*, vol. 6512, 2007, pp. 651214.

[24] M.K. Garvin, M.D. Abràmoff, X. Wu, S.R. Russell, T.L. Burns, and M. Sonka, "Automated 3-D intraretinal layer segmentation of macular spectral-domain optical coherence tomography images," *IEEE Transactions on Medical Imaging*, vol. 28, Sep. 2009, pp. 1436-1447.

[25] D.C. Fernandez, H.M. Salinas, and C.A. Puliafito, "Automated detection of retinal layer structures on optical coherence tomography images," *Opt. Express*, vol. 13, 2005, pp. 10200-10216.

[26] A. Mishra, A. Wong, K. Bizheva, and D.A. Clausi, "Intra-retinal layer segmentation in optical coherence tomography images.," *Opt. Express*, vol. 17, Dec. 2009, pp. 23719-23728.

[27] M.R. Hee, D. Huang, and E.A. Swanson, "Polarization-sensitive low-coherence reflectometer for birefringence characterization and ranging," *J. Opt. Soc. Am. A*, vol. 9, 1992, pp. 903-908.

[28] E. Götzinger, M. Pircher, W. Geitzenauer, C. Ahlers, B. Baumann, S. Michels, U. Schmidt-Erfurth, and C.K. Hitzenberger, "Retinal pigment epithelium segmentation by polarization sensitive optical coherence tomography," *Opt. Express*, vol. 16, Oct. 2008, pp. 16410-16422.

[29] A. Yazdanpanah, G. Hamarneh, B. Smith, and M. Sarunic, "Segmentation of Intra-Retinal Layers from Optical Coherence Tomography Images using an Active Contour Approach.," *IEEE Transactions on Medical Imaging*, Oct. 2010.

[30] M.V. Sarunic, A. Yazdanpanah, E. Gibson, J. Xu, Y. Bai, S. Lee, H.U. Saragovi, and M.F. Beg, "Longitudinal study of retinal degeneration in a rat using spectral domain optical coherence tomography," *Opt. Express*, vol. 18, 2010, pp. 23435-23441.

[31] T.F. Chan and L.A. Vese, "Active contours without edges," *IEEE Transactions on Medical Imaging*, vol. 10, Jan. 2001, pp. 266-277.

[32] A.F. Fercher, W. Drexler, C.K. Hitzenberger, and T. Lasser, "Optical coherence tomography (OCT): principles of operation, technology, indications in vitreoretinal imaging and interpretation of results.," *Reports on Progress in Physics*, vol. 66, Jan. 2003, pp. 239-303.

[33] J.A. Izatt and M.A. Choma, "Optical Coherence Tomography: Technology and Applications," W. Drexler and J.G. Fujimoto, eds., New York: Springer Berlin Heidelberg, 2008.

[34] M. Sarunic, "Advanced systems design for Fourier domain optical coherence tomography," PhD Thesis, Duke University, 2006.

[35] J.M. Schmitt, S.H. Xiang, and K.M. Yung, "Speckle reduction techniques," *Handbook of optical coherence tomography*, B.E. Bouma and G.J. Tearney, Eds., Marcel Dekker, 2002.

[36] J.M. Schmitt, S.H. Xiang, and K.M. Yung, "Speckle in Optical Coherence Tomography," *Biomedical Optics*, vol. 4, 1999, pp. 95-105.

[37] M.E. Brezinski, *Optical coherence tomography: principles and applications*, Academic Press, 2006.

[38] A. Pižurica, L. Jovanov, B. Huysmans, V. Zlokolica, P.D. Keyser, F. Dhaenens, and W. Philips, "Multiresolution Denoising for Optical Coherence Tomography : A Review and Evaluation," *Current Medical Imaging Reviews*, vol. 4, pp. 270-284(15).

[39] A. Achim, P. Tsakalides, and A. Bezerianos, "SAR Image Denoising via Bayesian Wavelet Shrinkage Based on Heavy-Tailed Modeling," *IEEE Transactions on Geoscience and Remote Sensing*, vol. 41, 2003, pp. 1773-1784.

[40] S. Gupta, R.C. Chauhan, and S.C. Sexana, "Wavelet-based statistical approach for speckle reduction in medical ultrasound images," *Medical & Biological Engineering & Computing*, vol. 42, 2004, pp. 189-192.

[41] O.V. Michailovich and A. Tannenbaum, "Despeckling of medical ultrasound images.," *IEEE Transactions on Ultrasonics, Ferroelectrics, and Frequency Control,* vol. 53, Jan. 2006, pp. 64-78.

[42] P. Cimalla, J. Walther, and E. Koch, "Investigations of the intravascular backscattering distribution of light in optical coherence tomography," *Biomedicine*, vol. 7554, 2010, pp. 755406,1-8.

[43] C.-wei Lu, C.-kuang Lee, M.-tsan Tsai, Y.-ming Wang, and C.C. Yang, "Measurement of the hemoglobin oxygen saturation level with spectroscopic spectral-domain optical coherence tomography," *Optics Letters*, vol. 33, 2008, pp. 416-418.

[44] D.J. Faber, E.G. Mik, M.C.G. Aalders, and T.G. Van Leeuwen, "Toward assessment of blood oxygen saturation by spectroscopic optical coherence tomography," *Optics Letters*, vol. 30, 2005, pp. 1015-1017.

[45] M. Young, S. Lee, E. Gibson, K. Hsu, M.F. Beg, P.J. Mackenzie, and M.V. Sarunic, "Morphometric analysis of the optic nerve head with optical coherence tomography," *Optical Coherence Tomography and Coherence Domain Optical Methods in Biomedicine*, 2010, pp. 75542L-6.

[46] K. Michael, W. Andrew, and T. Demetri, "Snakes: Active Contour Models," *International Journal of Computer Vision*, vol. 1, 1987, pp. 321-331.

[47] N. Hraiech, D. Weinland, and K. Hamrouni, "An Active Contour Model Based on Splines and Separating Forces to Detect the Left Ventricle in Scintigraphic Images," *International Conference on Machine Intelligence*, 2005, pp. 417-420.

[48] T. McInerney and D. Terzopoulos, "Topologically adaptable snakes," *Proceedings of IEEE International Conference on Computer Vision*, 1995, pp. 840-845.

[49] T. McInerney and D. Terzopoulos, "T-snakes: topology adaptive snakes.," *Medical Image Analysis*, vol. 4, Jun. 2000, pp. 73-91.

[50] S. Osher and S. James A, "Fronts propagating with curvature-dependent speed: Algorithms based on Hamilton-Jacobi formulations," *Journal of Computational Physics*, vol. 79, 1988, pp. 12-49.

[51] J.A. Sethian, *Level Set Methods and Fast Marching Methods: Evolving Interfaces in Computational Geometry, Fluid Mechanics,Computer Vision, and Materials Science*, Cambridge University Press, 1999.

[52] C. Xu, D. Pham, and J. Prince, "Handbook of Medical Imaging:Medical Image Processing and Analysis," M. Sonka and M. Fitzpatrick, eds., Bellingham, Washington: SPIE- The International Society for Optical Engineering, 2000.

[53] L.D. Cohen, "On Active Contour Models and Balloons," *CVGIP: Image Understanding*, vol. 53, pp. 211-218.

[54] C. Xu and J.L. Prince, "Snakes, shapes and gradient vector flow," *IEEE Transactions on Image Processing*, vol. 7, 1998, pp. 359-369.

[55] C. Xu and J.L. Prince, "Gradient vector flow: a new external force for snakes," *Computer Vision and Pattern Recognition, IEEE Computer Society Conference on*, 1997, pp. 66-71.

[56] R. Malladi, J. a Sethian, and B.C. Vemuri, "Shape modeling with front propagation: a level set approach," *IEEE Transactions on Pattern Analysis and Machine Intelligence*, vol. 17, 1995, pp. 158-175.

[57] V. Caselles, R. Kimmel, and S. Guillermo, "Geodesic active contours," *International Journal of Computer Vision*, vol. 22, Jan. 1997, pp. 61-79.

[58] R. Malladi, J.A. Sethian, and B.C. Vemuri, "Evolutionary fronts for topology-independent shape modeling and recovery," *in Proc. 3rd Eur. Conf. Computer Vision*, 1994, pp. 3-13.

[59] R. Malladi, J.A. Sethian, and B.C. Vemuri, *A topology-independent shape modeling scheme*, SPIE Vol. 2031 Geometric Methods in Computer Vision II, 1993. pp. 246-258.

[60] V. Caselles, F. Catté, T. Coll, and F. Dibos, "A geometric model for active contours in image processing," *Numerische Mathematik*, vol. 66, 1993, pp. 1–31.

[61] D. Mumford and J. Shah, "Optimal Approximations by Piecewise Smooth Functions and Associated Variational Problems'," *Communications on Pure and Applied Mathematics*, vol. 42, 1989, pp. 577-685.

[62] C. Li, C. Xu, and M. Fox, "Level Set Evolution without Re-Initialization: A New Variational Formulation," *IEEE Computer Society Conference on Computer Vision and Pattern Recognition (CVPR'05)*, 2005, pp. 430-436.

[63] J. Rao, G. Hamarneh, and R. Abugharbieh, "Adaptive contextual energy parameterization for automated image segmentation," *ISVC: Proceedings of the 5th International Symposium on Advances in Visual Computing*, 2009, pp. 1089–1100.

[64] J. Rao, R. Abugharbieh, and G. Hamarneh, "Adaptive regularization for image segmentation using local image curvature cues," *Computer Vision– ECCV 2010*, 2010, pp. 651–665.

[65] L. Tang, G. Hamarneh, and R. Abugharbieh, "Reliability-Driven, Spatially-Adaptive Regularization for Deformable Registration," *Workshop on Biomedical Image Registration*, 2010, pp. 173–185.

[66] W.F. Ames, *Numerical methods for partial differential equations*, Boston: Academic Press, 1992.

[67] A. Mansouri, A. Mitiche, and C. Vazquez, "Multiregion competition: A level set extension of region competition to multiple region image partitioning," *Computer Vision and Image Understanding*, vol. 101, Mar. 2006, pp. 137-150.

[68] B. Smith, A. Saad, G. Hamarneh, and T. Möller, "Recovery of Dynamic PET Regions via Simultaneous Segmentation and Deconvolution," *MICCAI Workshop on Analysis of Functional Medical Image Data (MICCAI functional)*, 2008, pp. 33-40.

[69] G. Aubert and L. Vese, "A variational method in image recovery," *SIAM Journal on Numerical Analysis*, vol. 34, pp. 1948-1979.

[70] L. Rudin, S. Osher, and E. Fatemi, "Nonlinear total variation based noise removal algorithms," *Physica D: Nonlinear Phenomena*, vol. 60, Nov. 1992, pp. 259-268.

[71] C. Pluempitiwiriyawej, J.M.F. Moura, Y.-J.L. Wu, and C. Ho, "STACS: new active contour scheme for cardiac MR image segmentation," *IEEE Transactions on Medical Imaging*, vol. 24, May. 2005, pp. 593-603.

[72] K.H. Kim, G.N. Maguluri, K. Cusato, R.B. Barlow, and J.F.D. Boer, "Monitoring mouse retinal degeneration with high-resolution spectral-domain optical coherence tomography," *Journal of Vision*, vol. 8, 2008, pp. 1-11.

[73] A. D. Huang, E. Swanson, C. Lin, J. Schuman, W. Stinson, W. Chang, M. Hee, T. Flotte, K. Gregory, C. Puliafito and J. Fujimoto, "Optical coherence tomography," *Science*, vol. 254, 1991, pp. 1178-1181.

[74] J.M. Schmitt, S.H. Xiang, and K.M. Yung, "Speckle in Optical Coherence Tomography," *Journal of Biomedical Optics*, vol. 4, 1999, pp. 95-105.

[75] M. Gargesha, M.W. Jenkins, A.M. Rollins, and D.L. Wilson, "Denoising and 4D visualization of OCT images.," *Opt. Express*, vol. 16, Aug. 2008, pp. 12313-12333.

[76] S.E. Jones, B.R. Buchbinder, and I. Aharon, "Three-dimensional mapping of cortical thickness using Laplace's Equation," *Human Brain Mapping*, vol. 11, Sep. 2000, pp. 12-32.

[77] D. Adalsteinsson, "A Fast Level Set Method for Propagating Interfaces," *Journal of Computational Physics*, vol. 118, 1995, pp. 269 - 277.

[78] J.A. Sethian, "Level Set Methods and Fast Marching Methods:," *Evolving Interfaces in Computational Geometry, Fluid Mechanics, Computer Vision, and Materials Science.*, Cambridge, U.K.: Cambridge Univ., 1999.

[79] D. Peng, "A PDE-Based Fast Local Level Set Method," *Journal of Computational Physics*, vol. 155, Nov. 1999, pp. 410-438.

[80] R. Malladi, J. Sethian, and B. Vemuri, "Shape modeling with front propagation: A level set approach," *IEEE Transactions on Pattern Analysis and Machine Intelligence*, vol. 17, 1995, pp. 158-175.

[81] R.T. Whitaker, "A level-set approach to 3D reconstruction from range data," *International Journal of Computer Vision*, vol. 29, 1998, pp. 203–231.

[82] C. Mcintosh and G. Hamarneh, "Is a single energy functional sufficient? Adaptive energy functionals and automatic initialization," *Medical Image Computing and Computer-Assisted Intervention (MICCAI)*, 2007, pp. 503-510.

[83] C. McIntosh and G. Hamarneh, "Optimal Weights for Convex Functionals in Medical Image Segmentation," *ISVC: Proceedings of the 5th International Symposium on Advances in Visual Computing*, vol. 5871, 2009, pp. 1079–1088.

[84] D. Anguelov, B. Taskar, V. Chatalbashev, D. Koller, D. Gupta, G. Heitz, and A.Y. Ng, "Discriminative learning of Markov random fields for segmentation of 3D scan data," *Proceedings of the IEEE Computer Society Conference on Computer Vision and Pattern Recognition (CVPR)*, vol. 2, 2005, pp. 169-176.

[85] T. Finley and T. Joachims, "Training Structural SVMs when Exact Inference is Intractable," *of the 25th International Conference on Machine Learning*, 2008, pp. 304-311.

[86] M. Szummer, P. Kohli, and D. Hoiem, "Learning CRFs using Graph Cuts," *Proceedings of the 10th European Conference on Computer Vision*, 2008, pp. 582-595.

[87] B. Taskar, D. Koller, and C. Guestrin, "Learning Structured Prediction Models : A Large Margin Approach," *Proceedings of the 22nd International Conference on Machine Learning*, 2005, pp. 896-903.

[88] V. Kolmogorov and Y. Boykov, "Applications of parametric maxflow in computer vision," *ICCV 2007. IEEE 11th International Conference on*, 2007, pp. 1-8.

[89] J. Rao, G. Hamarneh, and R. Abugharbieh, "Adaptive Contextual Energy Parameterization," *ISVC '09: Proceedings of the 5th International Symposium on Advances in Visual Computing*, 2009, pp. 1089-1100.

[90] X. Bresson, S. Esedoḡlu, P. Vandergheynst, J.-P. Thiran, and S. Osher, "Fast Global Minimization of the Active Contour/Snake Model," *Journal of Mathematical Imaging and Vision*, vol. 28, 2007, pp. 151-167.

[91] M. Nikolova, S. Esedoglu, and T.F. Chan, "Algorithms for Finding Global Minimizers of Image Segmentation and Denoising Models," *SIAM Journal on Applied Mathematics*, vol. 66, 2006, pp. 1632.

[92] T. Pock, T. Schoenemann, G. Graber, H. Bischof, and D. Cremers, "A Convex Formulation of Continuous Multi-Label Problems," *European Conference on Computer Vision (ECCV)*, 2008, pp. 1-14.

[93] D. Cremers, F.R. Schmidt, and F. Barthel, "Shape priors in variational image segmentation: Convexity, Lipschitz continuity and globally optimal solutions," *IEEE Conference on Computer Vision and Pattern Recognition (CVPR)*, 2008, pp. 1-6.

APPENDICES

Appendix A:

Euler Lagrange based evolution equations of the Functional E

In this work, the energy functional defined by (4-14) is minimized using the calculus of variations, which states that the Euler-Lagrange equation (A-1) provides a sufficient condition for a stationary point of the functional. Applying the Euler-Lagrange equation to our energy functional (4-14) yields:

$$\frac{\partial F}{\partial \phi_j} - \frac{d}{dx}\left(\frac{\partial F}{\partial \phi_{jx}}\right) - \frac{d}{dy}\left(\frac{\partial F}{\partial \phi_{jy}}\right) = 0, \tag{A-1}$$

where:

$$F = \lambda_I \sum_{i=1}^{R}\left[(I - \mu_i)^2 \chi_i\right] + \sum_{i=1}^{R-1}\left[A_i \delta(\phi_i)\mid \nabla \phi_i \mid + \frac{\lambda''_R}{2}(\mid \nabla \phi_i \mid -1)^2\right]. \tag{A-2}$$

Note that the Euler-Lagrange equation can be treated independently for each ϕ_j.

The partial derivative of F in (A-2) with respect to ϕ_j, ϕ_{jx}, and ϕ_{jy} respectively are:

$$\frac{\partial F}{\partial \phi_j} = \lambda_I \sum_{i=1}^{R}\left[(I - \mu_i)^2 \frac{\partial \chi_i}{\partial \phi_j}\right] + A_j \delta'(\phi_j)\mid \nabla \phi_j \mid, \tag{A-3}$$

$$\frac{\partial F}{\partial \phi_{jx}} = A_j \delta(\varphi_j)\frac{\phi_{jx}}{\mid \nabla \phi_j \mid} + \lambda''_R\left(\mid \nabla \phi_j \mid -1\right)\frac{\phi_{jx}}{\mid \nabla \phi_j \mid}, \tag{A-4}$$

$$\frac{\partial F}{\partial \phi_{jy}} = A_j \delta(\phi_j) \frac{\phi_{jy}}{|\nabla \phi_j|} + \lambda''_R \left(|\nabla \phi_j| - 1\right) \frac{\phi_{jy}}{|\nabla \phi_j|}, \tag{A-5}$$

where $\delta' = \partial \delta / \partial \phi_j$.

Taking the derivative of (A-4) with respect to x, we have:

$$\frac{d}{dx}(\frac{\partial F}{\partial \phi_{jx}}) = A_{jx} \delta(\phi_j) \frac{\phi_{jx}}{|\nabla \phi_j|} + A_j \delta'(\phi_j) \frac{\phi_{jx}^2}{|\nabla \phi_j|} + A_j \delta(\phi_j) \frac{d}{dx}\left(\frac{\phi_{jx}}{|\nabla \phi_j|}\right)$$
$$+ \lambda''_R \left[\frac{d}{dx}\phi_{jx} - \frac{d}{dx}\left(\frac{\phi_{jx}}{|\nabla \phi_j|}\right)\right]. \tag{A-6}$$

Similarly, the derivative of (A-5) with respect to y is:

$$\frac{d}{dy}(\frac{\partial F}{\partial \phi_{jy}}) = A_{jy} \delta(\phi_j) \frac{\phi_{jy}}{|\nabla \phi_j|} + A_j \delta'(\phi_j) \frac{\phi_{jy}^2}{|\nabla \phi_j|} + A_j \delta(\phi_j) \frac{d}{dy}\left(\frac{\phi_{jy}}{|\nabla \phi_j|}\right)$$
$$+ \lambda''_R \left[\frac{d}{dy}\phi_{jy} - \frac{d}{dy}\left(\frac{\phi_{jy}}{|\nabla \phi_j|}\right)\right]. \tag{A-7}$$

By substituting the terms (A-3), (A-6), and (A-7) in (A-1), and re-arranging slightly, the Euler-Lagrange corresponding to the functional (4-2) is defined as:

$$\lambda_I \sum_{i=1}^{R} \left[(I - \mu_i)^2 \frac{\partial \chi_i}{\partial \phi_j}\right] - \left[\nabla A_j \cdot \frac{\nabla \phi_j}{|\nabla \phi_j|} + A_j \operatorname{div}\left(\frac{\nabla \phi_j}{|\nabla \phi_j|}\right)\right] \delta(\phi_j)$$
$$- \lambda''_R \left[\Delta \phi_j - \operatorname{div}\left(\frac{\nabla \phi_j}{|\nabla \phi_j|}\right)\right] = 0. \tag{A-8}$$

In the equation above we made use of the fact that:

$$|\nabla \phi_j(x, y)| = \sqrt{\phi_{jx}^2 + \phi_{jy}^2},$$

$$\frac{d}{dx}\left(\frac{\phi_{jx}}{|\nabla \phi_j|}\right) + \frac{d}{dy}\left(\frac{\phi_{jy}}{|\nabla \phi_j|}\right) = \text{div}\left(\frac{\nabla \phi_j}{|\nabla \phi_j|}\right), \qquad \text{(A-9)}$$

$$A_{jx}\frac{\phi_{jx}}{|\nabla \phi_j|} + A_{jy}\frac{\phi_{jy}}{|\nabla \phi_j|} = \nabla A_j \cdot \frac{\nabla \phi_j}{|\nabla \phi_j|},$$

where '·' is a vector dot product.